INTERIM REPORT

Advanced Magnetometer System
Task II

SERDP Project MR-2646

AUGUST 2019

Dr. Rui Zhang
Dr. Rahul Mhaskar
Geometrics

SERDP
DOD ▪ EPA ▪ DOE

REPORT DOCUMENTATION PAGE

Form Approved
OMB No. 0704-0188

1. REPORT DATE *(DD-MM-YYYY)*	**2. REPORT TYPE**	**3. DATES COVERED** *(From - To)*
09/08/2019	SERDP Interim Report	9/26/2016 - 9/26/2021

4. TITLE AND SUBTITLE

Advanced Magnetometer System - Task II

5a. CONTRACT NUMBER
16-C-0010

5b. GRANT NUMBER

5c. PROGRAM ELEMENT NUMBER

6. AUTHOR(S)
Dr. Rui Zhang
Dr. Rahul Mhaskar

5d. PROJECT NUMBER
MR-2646

5e. TASK NUMBER

5f. WORK UNIT NUMBER

7. PERFORMING ORGANIZATION NAME(S) AND ADDRESS(ES)
GEOMETRICS, INC.
2190 Fortune Drive
San Jose, CA, 95131

8. PERFORMING ORGANIZATION REPORT NUMBER
MR-2646

9. SPONSORING/MONITORING AGENCY NAME(S) AND ADDRESS(ES)
Strategic Environmental Research and Development Program (SERDP)
4800 Mark Center Drive, Suite 16F16
Alexandria, VA 22350-3605

10. SPONSOR/MONITOR'S ACRONYM(S)
SERDP

11. SPONSOR/MONITOR'S REPORT NUMBER(S)
MR-2646

12. DISTRIBUTION/AVAILABILITY STATEMENT
DISTRIBUTION STATEMENT A. Approved for public release: distribution unlimited.

13. SUPPLEMENTARY NOTES

14. ABSTRACT
Scalar magnetometers and Time-Domain Electromagnetic (TDEM) systems are proven and effective technologies used extensively in the field to detect, discriminate and classify unexploded ordnance (UXO). However, it has not been possible to simultaneously run both sensors in close vicinity of each other due to the interruption of the magnetometer operation by the EM pulses. We propose a method minimizing the EM pulse interruption by developing advanced digital signal processing (DSP) techniques to drive the scalar magnetometer. The method requires the angle information of the magnetic field, which cannot be obtained using commercial scalar magnetometers. In the first phase of the project, we demonstrate the capability of extracting the field angle information based on intrinsic operating parameters of the magnetometer. Better than 0.02° sensitivity can be achieved in angle measurement at the optimal orientation of the magnetic field with a measurement time of 100 ms. The demonstrated angle measurement shows that it is possible to achieve the fast tracking of the EM pulse with our advanced scalar atomic magnetometer system.

15. SUBJECT TERMS
Scalar Atomic Magnetometer, Time-Domain Electromagnetic System, Digital Signal Processing

16. SECURITY CLASSIFICATION OF:			**17. LIMITATION OF ABSTRACT**	**18. NUMBER OF PAGES**	**19a. NAME OF RESPONSIBLE PERSON**
a. REPORT	**b. ABSTRACT**	**c. THIS PAGE**			Rui Zhang
UNCLASS	UNCLASS	UNCLASS	UNCLASS	36	**19b. TELEPHONE NUMBER** *(Include area code)* 408-954-0522

Contents

List of Figures

List of Acronyms

AOM	Acousto-Optic Modulator
Cs	Cesium
DBR	Distributed Bragg Reflector
DC	Direct Current
DPLL	Digital Phase Locked Loop
DSP	Digital Signal Processing
EM	Electromagnetic
ESTCP	Environmental Security Technology Certification Program
FPGA	Field-programmable Gate Array
FWHM	Full Width at Half Maximum
Hz	Hertz
kHz	kilohertz
MFAM	Refers to Miniature Scalar Magnetometer
ms	millisecond
nT	nanotesla
pT	picotesla
μs	microsecond
μT	microtesla
OD	Optical Density
PI	Proportional-Integral
PLL	Phase-Locked Loop
rms	Root Mean Square
SERDP	Strategic Environmental Research and Development Program
TDEM	Time-Domain Electromagnetic
UXO	Unexploded Ordnance
VCSEL	Vertical Cavity Surface Emitting Laser
3-D	Three-Dimensional

List of Keywords

Scalar Atomic Magnetometer, Time-Domain Electromagnetic System, Digital Signal Processing

GEOMETRICS
Innovation • Experience • Results
2190 Fortune Drive, San Jose, CA 95131 USA • Tel (408) 954-0522 • Fax (408) 954-0902

Fast Recovery of Magnetometer Operation in Presence of Electromagnetic Pulses

Abstract

Scalar magnetometers and Time-Domain Electromagnetic (TDEM) systems are proven and effective technologies used extensively in the field to detect, discriminate and classify unexploded ordnance (UXO). However, without complicated interleaving method [1], it is not possible to simultaneously run both sensors in the close vicinity to each other due to the interruption of the magnetometer operation by the EM pulses. We propose a method minimizing the EM pulse interruption by developing advanced digital signal processing (DSP) techniques to drive the scalar magnetometer. In the first phase of the project, we demonstrated the capability of extracting the field angle information based on intrinsic operating parameters of the magnetometer. In the second phase, we show that the magnetometer can respond to a magnetic signal one millisecond after the EM pulse is turned off. When integrated with the angle measurement method developed in the first phase, the DSP technique can even enable the magnetometer to operate during the EM pulse. Simultaneous operation of the advanced magnetometer system with a commercial TDEM system was also successfully verified, enabling innovate hybrid magnetometer-TDEM systems.

Project Objectives

The objective of the MR-2646 project is to enable the integration of miniature laser-pumped cesium magnetometers with TDEM systems by improving the magnetometer to function in presence of an EM transmitter. This project relates to MRSON-16-01, Detection, Classification, and Remediation of Military Munitions Underwater. By developing technologies necessary to integrate a magnetometer array with an advanced TDEM system, this project addresses sensor development, platform integration, and analysis methodologies necessary for efficient large-scale collection of field data during the detailed survey phase and particularly in an underwater environment.

Scalar atomic magnetometers rely on the resonant Larmor precession of atomic spins to measure the magnitude of the magnetic field [2]. A high-amplitude EM pulse can interrupt the magnetometer operation by collapsing the precession signal. It typically takes a few tens of milliseconds for the magnetometer to find the resonant Larmor frequency again. The recovery time can be greatly reduced, however, if the initial driving frequency is set to be close to the resonant Larmor frequency. This can be implemented using the advanced digital signal processing (DSP) solutions we have developed for driving a scalar magnetometer. The resonant Larmor frequency during the EM pulse can be calculated based on the vector sum of the EM pulse and the background magnetic field. The EM pulse at the location of the magnetometer can be calibrated and the magnitude of the background field is measured by the scalar magnetometer. If the angle information about the background field can also be obtained, we will be able to

implement the fast-recovery method of operating the scalar magnetometers in the presence of EM pulses.

Specific technical objectives are as follows:

1. Evaluate, through simulations and laboratory experiments, advanced methods of signal extraction in the scalar magnetometer instrument.
2. Implement advanced methods of operating the sensors to obtain rapid DC magnetometer measurements in the presence of a TDEM system.
3. Investigate the possibility of discrimination using DC magnetic measurements, probing in different directions, in a manner analogous to advanced TDEM systems.

This Interim Report addresses the second objective of the project. Key questions to be answered in this report: What is the slew-rate limit of our laser-pumped cesium magnetometer? Whether the proposed fast-recovery method works after the EM pulse is switched off? If so, what is the recovery time? Is the angle measurement method developed in the first phase of the project good enough to enable the fast-recovery during the EM pulse? EM pulses in TDEM systems typically have widths and separations of less than 10ms. Therefore, the recovery time of the magnetometers should be much less than 10ms and preferably less than 5ms for meaningful magnetic field measurements in the presence of a TDEM system. Successful realization of the fast-recovery during the EM pulses is also a pre-requisite of practical applications towards UXO discrimination methods proposed to be developed in the Task 3.

Technical Approach

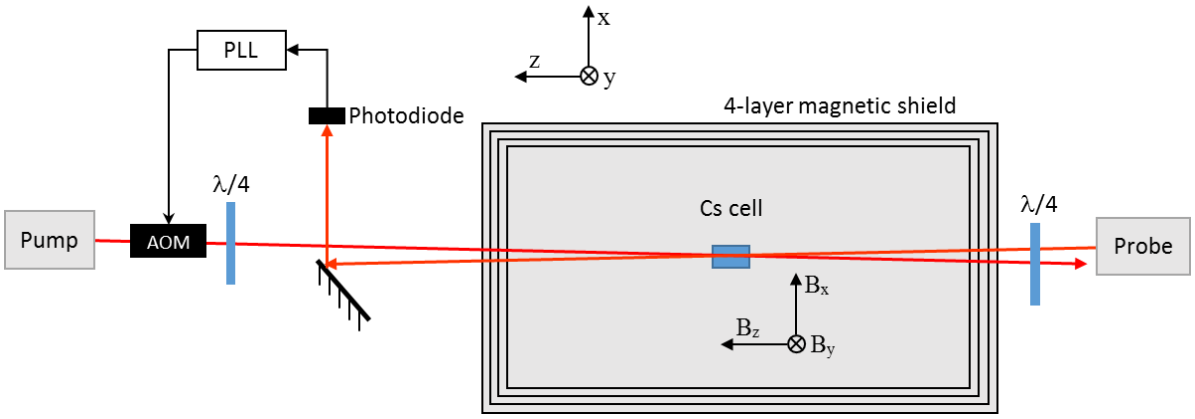

Figure 1 Schematic of the experimental setup of a bench-top scalar atomic magnetometer.

We use the bench-top scalar atomic magnetometer setup, shown schematically in Figure 1 to experimentally investigate the measurement concepts. A cuboid vapor cell containing Cs atoms is placed inside a 4-layer magnetic shield can. The cell is resistively heated to operating temperature. The pump and probe lights come from two Distributed Bragg Reflector (DBR) lasers and are circularly polarized with a quarter-wave-plate. The pump light is amplitude-modulated with an acousto-optic modulator (AOM). The angle between the two beams is about 1°. The fundamental operating principal of the magnetometer is based on the Bell-Bloom scheme [3]. The pump light periodically aligns atomic spins. The precession of the atomic spins in a magnetic field is detected by the counter-propagating probe beam. The transmitted probe light is detected and conditioned using electronics to determine the Larmor frequency and also control

the AOM driving frequency. Inside the shield can, the magnetic field in x, y and z directions can be independently controlled. We also place small coils (10 turns and less than 2 cm in diameter) next to the cell in both x and z directions for generating magnetic pulses.

1. Fundamental Slew Rate of the Magnetometer

a. Magnetic Response of Polarized Atomic Spin

The best solution for achieving simultaneous operation of a magnetometer and a TDEM system is for the magnetometer to have a slew rate that is high enough to follow the EM pulses. To investigate the fundamental slew rate of the magnetometer, we first study the dynamic response of polarized atomic ensemble spin, which generates the Larmor signal.

The experimental steps are as following. Initially the background magnetic field is set at 2 μT in x direction with the large Helmholtz coils. The AOM driving frequency is the resonant Larmor frequency at this field. After a short while (less than 3 ms), macroscopically polarized atomic spins build up and undergo Larmor precession, which is detected by the probe beam. At t = 0, a magnetic field of 10 μT, generated by the smaller coils, is switched on in less than 20 μs along the same direction. At the same time, the AOM driving frequency is turned off.

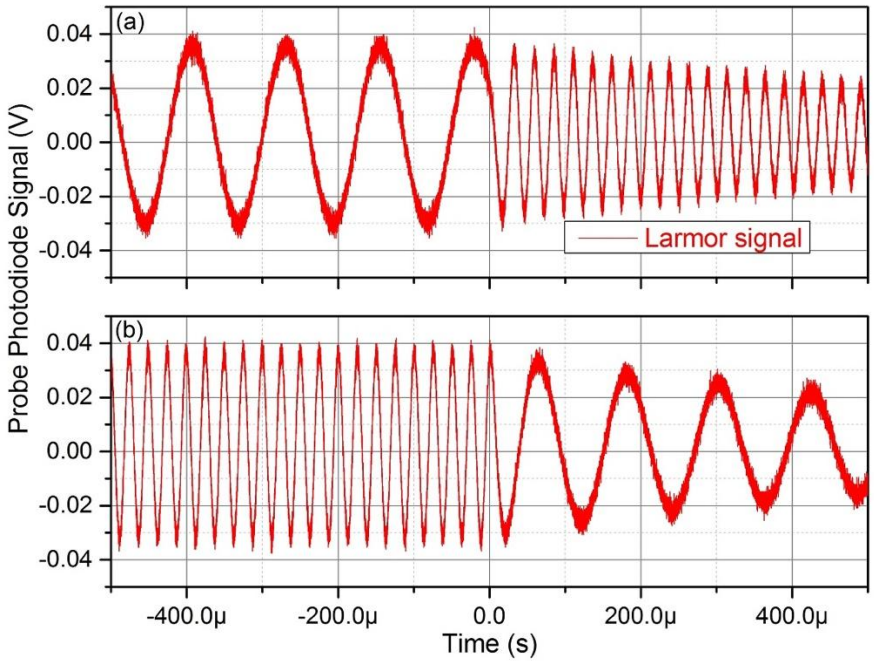

Figure 2 Magnetic response of polarized atomic spin. The magnetic field in x direction is changed from 2 μT to 12 μT in (a) and from 12 μT to 2 μT in (b) in less than 20 μs at t = 0.

The probe photodiode signal, representing the Larmor precession of the atomic spin, is shown in Figure 2 (a). As seen, the precession of the atomic spin follows the magnetic field pulse almost instantaneously. In Figure 2 (b), we change the magnetic field from 12 μT to 2 μT at t = 0. A similar result is observed. The demonstrated dynamic response of polarized atomic spin indicates that the slew rate of the atomic magnetometer is not limited by the fundamental physics.

b. Tuning of the Phase-Lock-Loop

As we saw in the previous section, the atomic spin can react to a sudden change of the magnetic field almost instantaneously. Therefore, the response of a Larmor-based atomic magnetometer is not limited by the fundamental physics. Rather it depends on the detailed implementation of the feedback loop in the driving electronics of the magnetometer. We use a commercially available digital phase-lock-loop (PLL) system as the feedback controller.

A typical implementation of the PLL involves three stages, schematically shown in Figure 3. The phase of the input probe photodiode signal is compared with a reference signal, generated by the local oscillator, at the phase detector stage. The output of the phase detector goes through a PI controller, which controls the frequency of the local oscillator.

The feedback loop of the PLL adjusts the frequency of the local oscillator such that there is a set phase difference between the local oscillator and the Larmor signal. This also ensures that the local oscillator has the same frequency as the input Larmor signal. The response of such a PLL-based magnetometer will depend on the time constants of both the phase detector and the PI controller. We use the smallest time constants (790 ns for the phase detector and 50 μs for the PI controller) for the following experiments in the fundamental slew rate investigation.

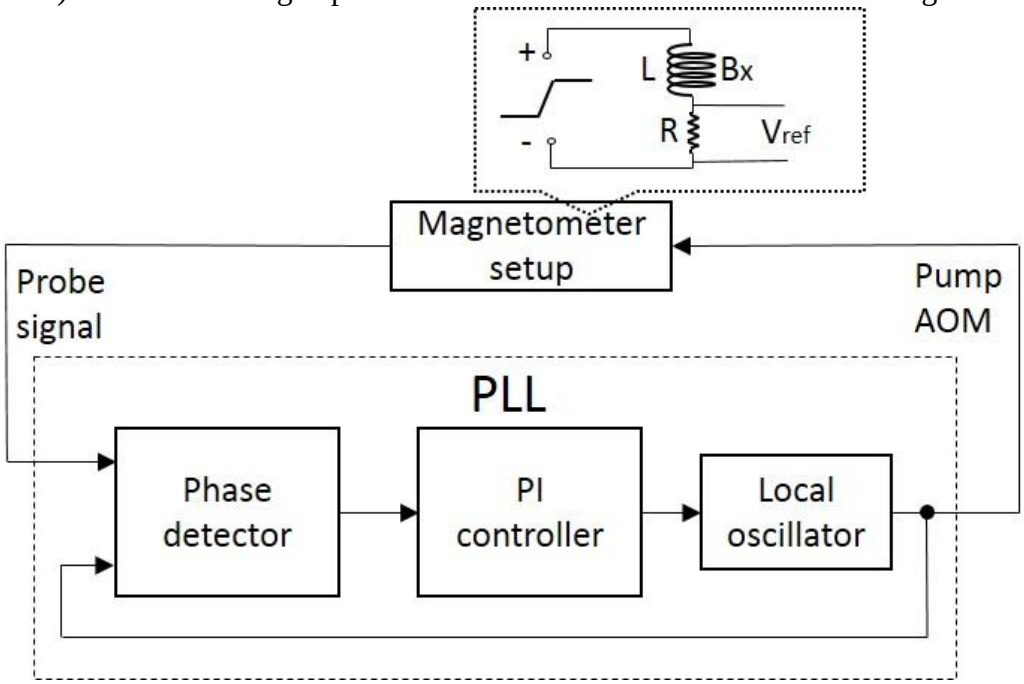

Figure 3 Block diagram showing the implementation of the PLL. The magnetometer setup is shown in Figure 1.

c. Limit of the Slew Rate of the Magnetometer

We test the slew rate of the magnetometer by ramping up a 50 μT magnetic field in x direction using the small coils as shown in Figure 3. A constant field of 60 μT is also applied along the same direction using the larger coils. The voltage across a pickup resistor in series with the small coils, reference voltage V_{ref}, indicates the actual magnetic field ramp. The slope of the ramp is varied. The probe photodiode signal, V_{ref}, and the magnetometer output are recorded during the ramp. The results are shown in Figure 4, with the photodiode signal (black curve) and V_{ref} (blue curve) given by the left axis and the magnetometer output (red curve) given by the right axis.

As seen, when the ramp time is more than 200 μs, the magnetometer output closely tracks the magnetic field ramp. When the ramp time is shortened to less than 100 μs, the PLL starts to lose lock, shown in Figure 4 (d), where the ramp time is only 90 μs. In this particular case, the magnetometer recovers its operation after the magnetic field is ramped back down to 60 μT. For short ramping time constants (< 100 μs), sometimes the PLL can completely lose the lock and never recover.

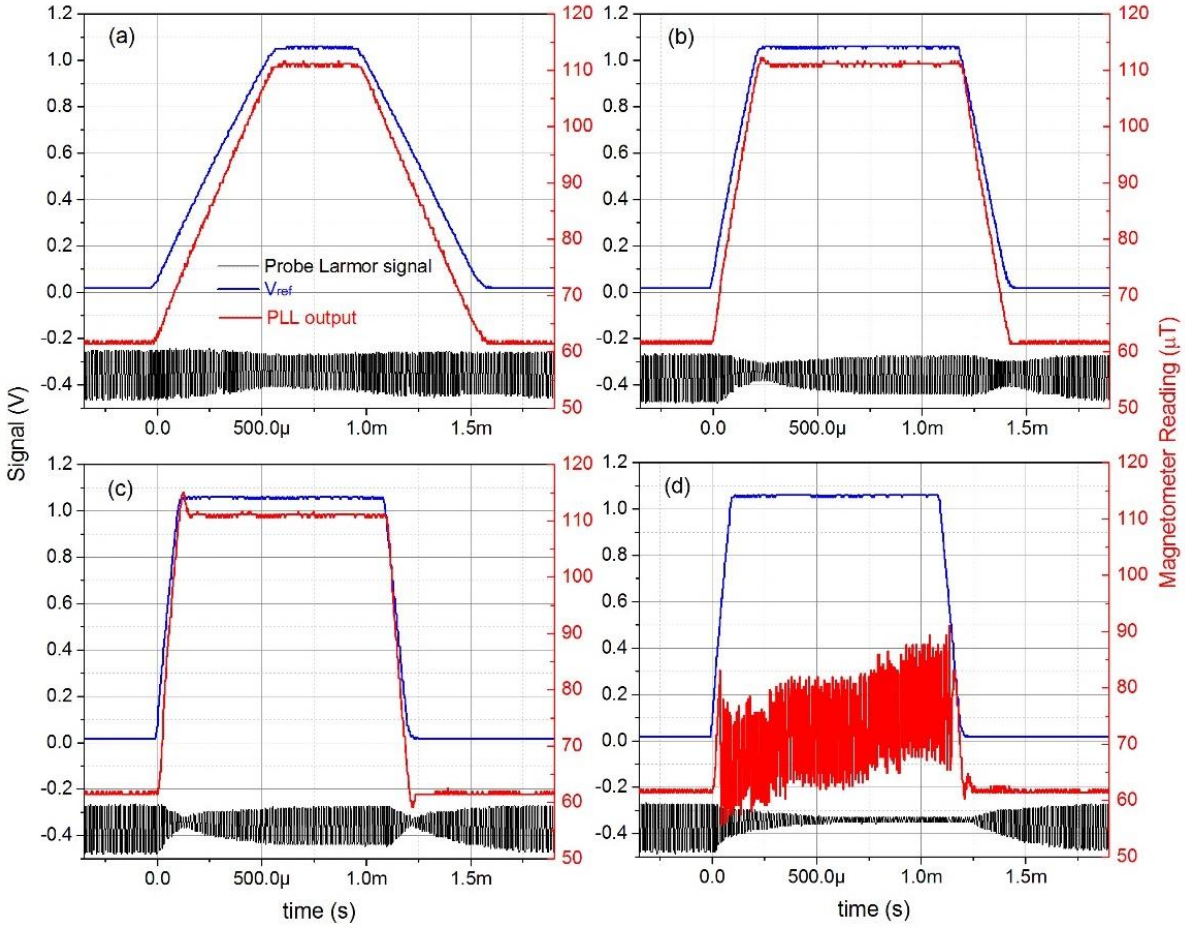

Figure 4 Response of the magnetometer to different rates of change of the magnetic field. (a), (b), (c) and (d) correspond to a 50 μT change in 500 μs, 200 μs, 100 μs and 90 μs, respectively. The photodiode signal (black) and V_{ref} (blue) are given by the left axis and the magnetometer output (red) is given by the right axis.

d. Bandwidth and Noise of the High-Slew-Rate Magnetometer

We measure the bandwidth of the magnetometer at different magnetic fields. The main magnetic field is set by the large coils in the x-direction. The small x-coils generate an oscillating magnetic field, the frequency of which is swept from 0.1 Hz to 80 kHz while its amplitude is fixed at 50 nT. We record the output of the magnetometer and measure the amplitude of the oscillating field as a function of its frequency. The normalized amplitude vs. frequency curve is plotted in Figure 5 (a). As seen, the bandwidth of the magnetometer at different magnetic fields is about the same. The hump around 10 kHz is due to the over-tuning of the PLL. The magnetometer noise is also measured by recording the magnetometer output for 5 minutes at a constant magnetic field.

The results are shown in Figure 5 (b). The rise of the magnetometer noise at high frequencies is mainly due to the increase in the PLL gain. We also notice that the low-frequency noise becomes worse at smaller magnetic fields. This is likely due to the small time constant of the PLL phase detector. At lower magnetic fields, the phase detector only averages over a few Larmor cycles, resulting in a larger phase error.

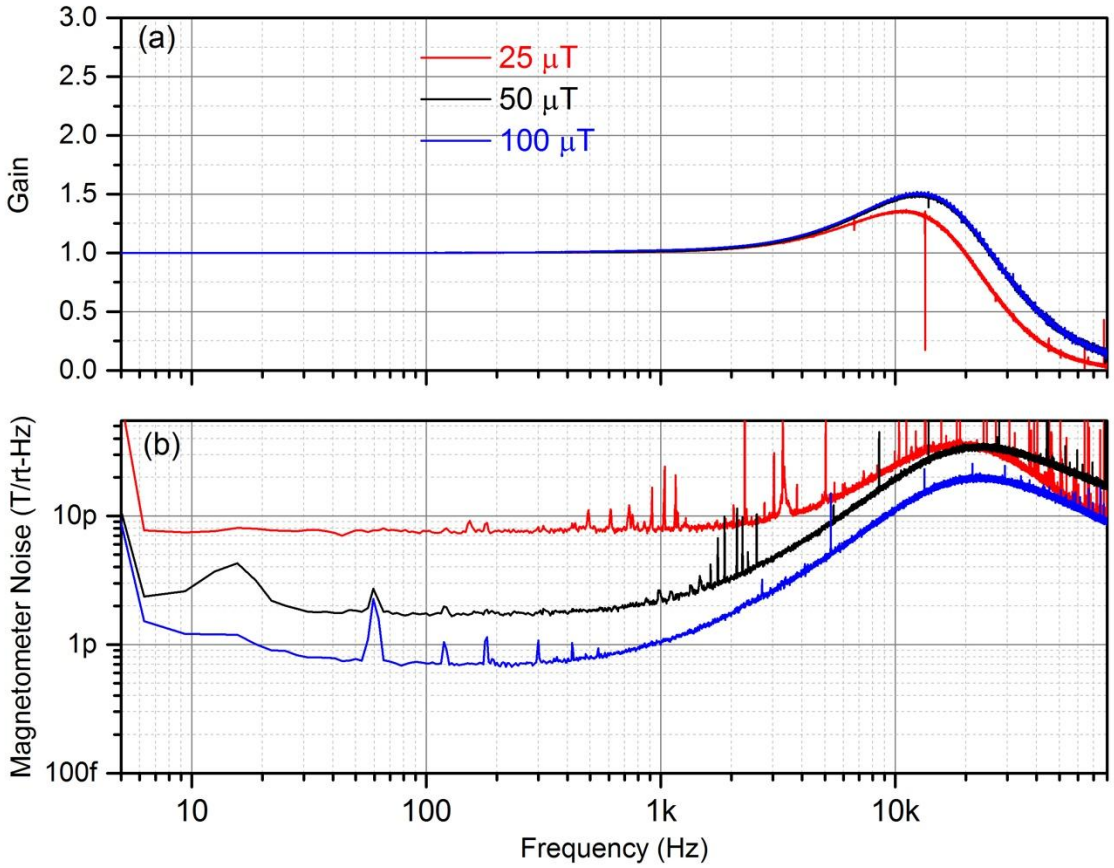

Figure 5 Bandwidth (a) and noise (b) of the high-slew-rate magnetometer at different magnetic fields.

e. Discussion

We demonstrate a slew rate of 500 μT/ms with a bench-top magnetometer. However, similarly high slew rates cannot be implemented with the commercial MFAM sensors. In the miniature MFAM sensors, vertical cavity surface emitting lasers (VCSEL) are used to minimize the size and power-consumption at the expense of increased laser frequency and detector noise. Electronics driving the operation of the MFAM exhibit higher noise compared to commercial PLL systems due to portability trade-offs.

As a result, the MFAM measurement noise is likely to be worse than that demonstrated in Figure 5 (b), especially around high frequencies. Combined with high PLL gains at high frequencies, it is hard to achieve a stable operation of PLL with MFAM sensors. In addition, many portable TDEM systems generate magnetic pulses exceeding the 500 μT/ms slew rate. Therefore, high-slew-rate portable magnetometers are not likely to be the solution achieving the simultaneous operation of magnetometers with TDEM systems. In the following section, we investigate the fast-recovery method immediately following the EM pulse.

2. Fast-recovery with a Pre-determined Larmor Frequency

When the EM pulses exceed the slew rate of the magnetometer, the magnetometer loses the track of the magnetic field and spends considerable time searching for the resonant Larmor frequency within its full dynamic range. The recovery time can be greatly reduced by scanning a limited span of frequencies close to the actual Larmor frequency. The dependence of the recovery time on the difference between the starting frequency of the scan and the actual Larmor frequency will also be investigated. As discussed in the previous section, the miniature MFAM sensors are unlikely to achieve a bandwidth of exceeding 10 kHz. Hence, the PLL is tuned for a bandwidth of around 2 kHz for the following experiments, which is feasible with the miniature sensors.

a. Characterization of the Method

The background magnetic field inside the shield can is set to B_x = 60.5 μT, corresponding to a resonant Larmor frequency of 212 kHz. Amplitude and phase of the Larmor signal across the resonant Larmor frequency are shown as the black and red curves, respectively, in Figure 6. To investigate the dependence of the PLL settle time on the separation between the starting pump modulation frequency and the actual Larmor frequency, the initial pump modulation frequency is set to be different from the resonant Larmor frequency before the PLL loop is closed. The tested starting pump frequencies are indicated by the blue lines in Figure 6. At t = 0, the PLL is enabled.

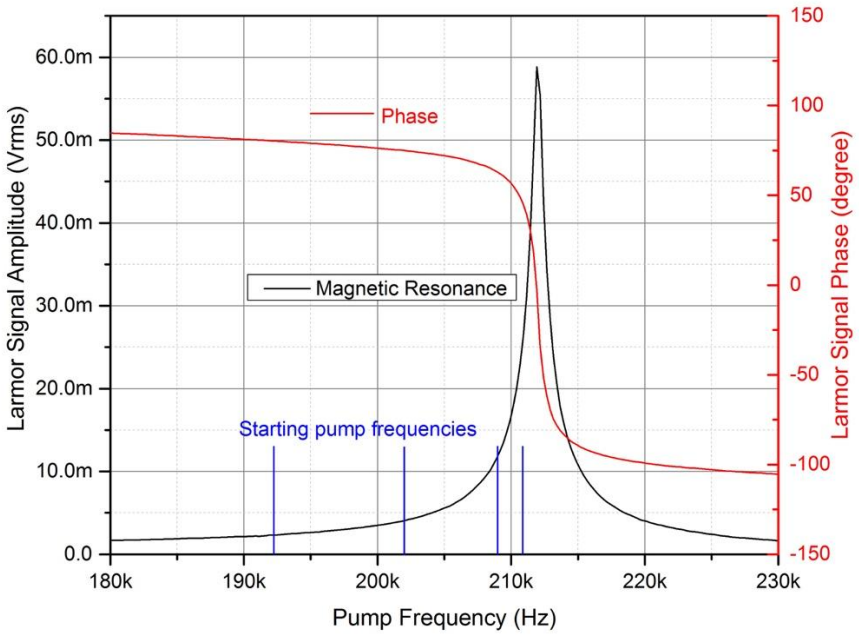

Figure 6 Magnetic resonance signal (black curve), its phase (red curve) and the starting pump frequencies (indicated by the blue lines).

The initial pump frequency is first set to be 1 kHz away from the resonant Larmor frequency, shown as the closest blue line to the magnetic resonance signal in Figure 6. The Larmor signal (black curve) and the magnetometer reading (red curve) are both recorded around t=0, and the magnetometer outputs the correct field reading within 1 ms as shown in Figure 7 (a). Meanwhile the Larmor signal also reaches steady state.

Notice that the field reading settles much faster than the signal amplitude because PLL measures the frequency, not the amplitude, of the Larmor signal. We also set the initial pump frequency to be 3 kHz, 10 kHz and 20 kHz away from the resonant Larmor frequency. Corresponding results are shown in Figure 7 (b), (c) and (d), respectively. As expected, the further away the initial pump frequency, the longer it takes for the magnetometer to recover its normal operation.

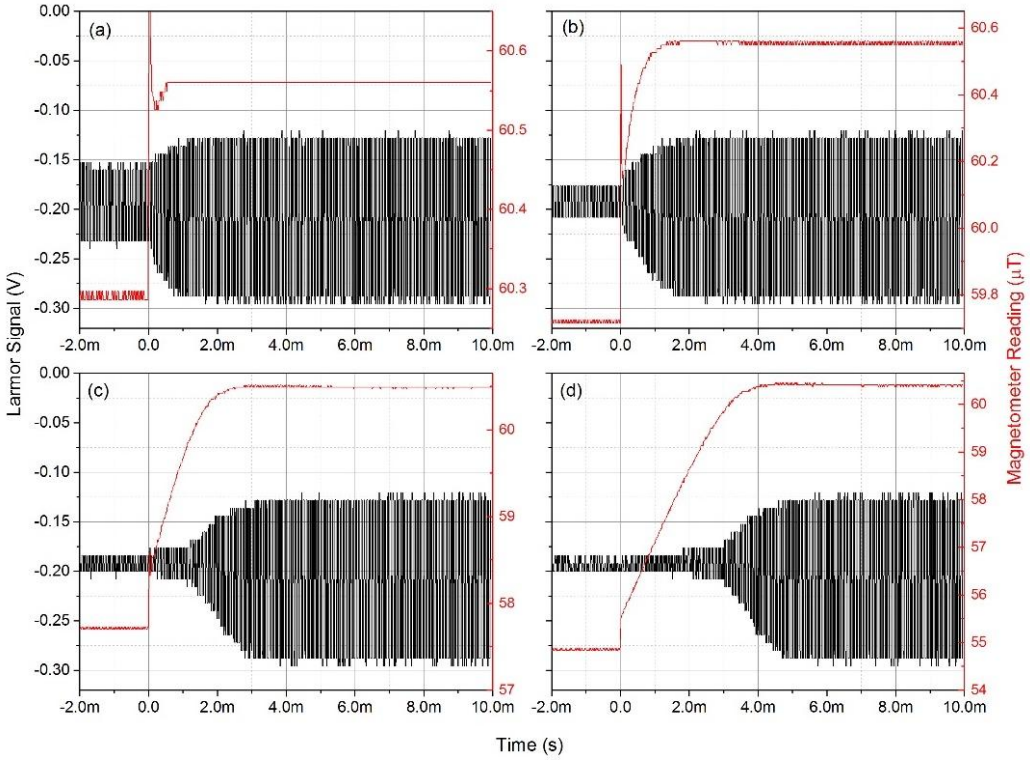

Figure 7 Reading of the magnetometer after the PLL is enabled (red curves). The initial pump modulation frequency is (a) 1 kHz, (b) 3 kHz, (c) 10 kHz and (d) 20 kHz away from the resonant Larmor frequency, corresponding to 4 blue lines in Figure 6. The probe Larmor signal detected by the photodiode is also shown as the black curve.

b. Fast-recovery after the EM Pulse

The previous experiment verifies that as long as the starting pump frequency is close to the actual Larmor frequency, the magnetometer recovers operation within 1ms. Therefore, the key to the fast-recovery of the magnetometer is to estimate the actual Larmor frequency. In most practical applications, only the magnetic field measurements immediately following the EM pulse are of interest. Since typical EM pulses last less than 10 ms, the Larmor frequency before an EM pulse provides a good estimate of the Larmor frequency after the EM pulse. In this case, we can use the Larmor frequency before the EM pulse as the starting pump frequency after the EM pulse.

With the commercial PLL system, we can limit the PLL range centered around a user-defined frequency. By applying this constraint, we can control the separation between the initial pump frequency and the actual Larmor frequency after the EM pulse is switched off. In the following experiment, we set the constant background magnetic field along polar 30° angle (Bz = 53 μT and Bx = -30 μT with large coils). This field orientation is on the edge of the dead zone of the magnetometer. Therefore, we expect the magnetometer to work even better in other background field directions.

The PLL center frequency is set to 210 kHz, corresponding to the Larmor frequency of the background magnetic field. The EM pulses are generated by the small x-coils with an amplitude of 220 μT and ramp time of 10 μs, well exceeding the slew rate of the magnetometer. The pulse train has a 50 Hz repetition rate with 25% duty cycle. During the EM pulses, V_{ref} and the magnetometer (PLL) output are recorded (Figure 8).

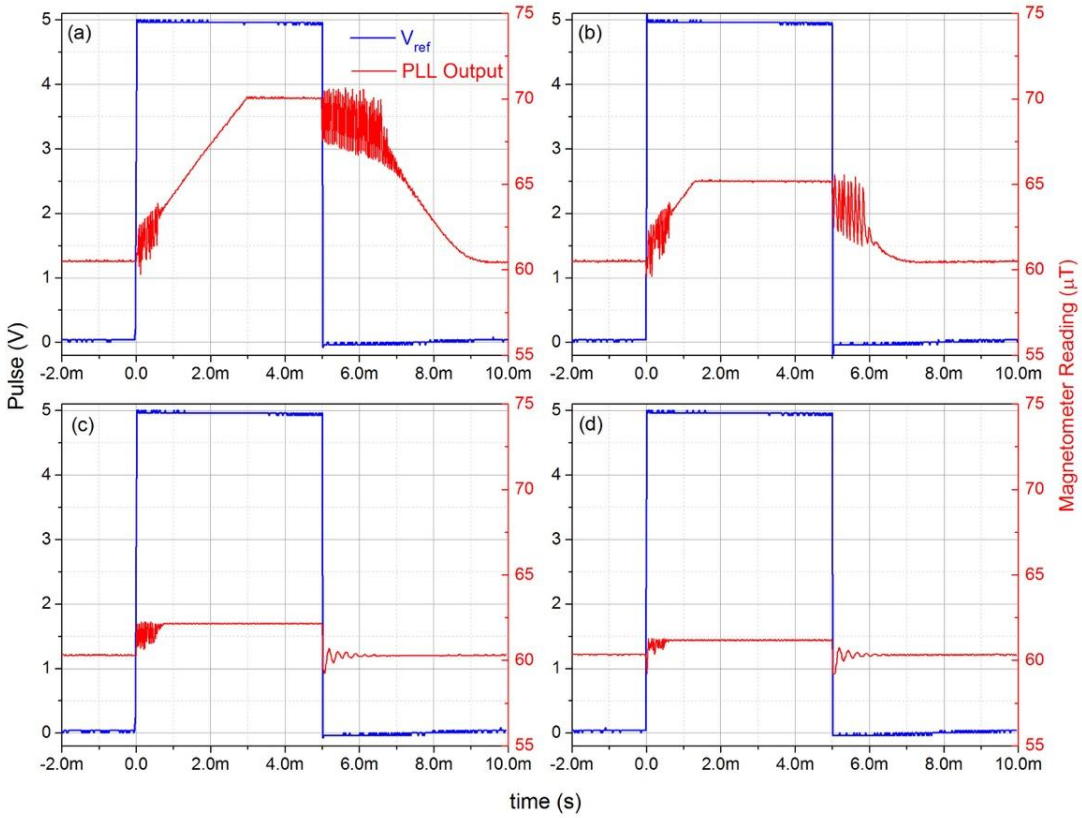

Figure 8 Fast-recovery of the magnetometer operation after EM pulses. The PLL range is set at (a) +/-35 kHz, (b) +/-17.5 kHz, (c) +/-7 kHz and (d) +/-3.5 kHz, from a center frequency of 210 kHz. The background magnetic field is set at 30° polar angle, Bz = 53 μT and Bx = -30 μT, with large coils. The magnetic pulse is generated by the small x-coils with amplitude of 220 μT and ramp time of 10 μs.

In Figure 8 (a), the PLL frequency range is set to be ± 35 kHz, corresponding to a magnetic field range of about ±10 μT. As seen, when the magnetic field pulse is switched on at t = 0, indicated by the V_{ref} curve, the PLL loses the track of the magnetic field. After about 3 ms, the PLL reaches its maximum range. The PLL frequency stays constant until the pulse is switched off at t = 5 ms. At this moment, the pump frequency, controlled by the PLL, is about 35 kHz away from the actual Larmor frequency. As seen, it takes almost 5 ms for the magnetometer to produce valid measurements after the pulse is switched off. In Figure 8 (b), (c) and (d, the PLL frequency range is set to ±17.5 kHz, ± 7 kHz and ± 3.5 kHz, respectively. Compared with the result in Figure 8 (a), when the initial pump frequency is closer to the actual Larmor frequency as shown in Figure 8 (b), the recovery of the magnetometer operation is faster. We verify that the damped oscillation in the magnetometer reading after the pulse is switched off, shown in Figure 8 (c) and (d), is a real magnetic signal. This is due to the under-damping of the induced current in the large coil circuit. By adding a resistor in series with the large coils, the large-coil driving

circuit can be over-damped. The change of behavior in the induced current is observed by the magnetometer.

To test the recovery of magnetometer operation, a small oscillating signal, about 200 nT peak to peak in the projected background field direction, is applied 2 ms after the EM pulse is switched off. The EM pulse train is set to 20 Hz repetition rate. The magnetometer reading and V_{ref} are recorded (Figure 9). As seen, the magnetometer regains its small-signal response after the EM pulse is switched off. The signal frequency is changed from 1 kHz to 200 Hz from Figure 9 (a) to (b). The measured signal amplitude does not change, indicating a magnetometer bandwidth of well above 1 kHz.

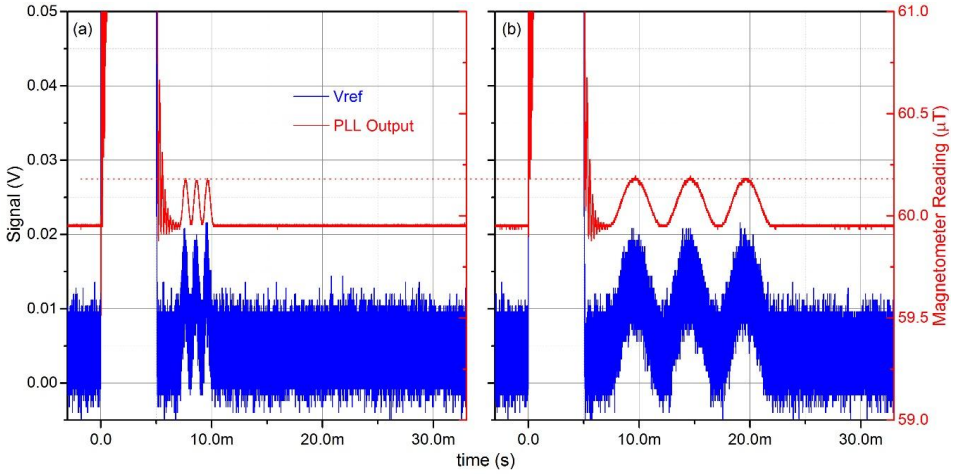

Figure 9 Measurement of a small oscillating signal 2ms after the magnetic pulse is switched off. The frequency of the signal is (a) 1 kHz and (b) 200 Hz.

c. Bandwidth and Noise

We also measure the bandwidth and the noise of the magnetometer with the current PLL parameters, as shown in Figure 10. Compared with the results shown in Figure 5, the magnetometer performance is not affected by the magnitude of the background magnetic field.

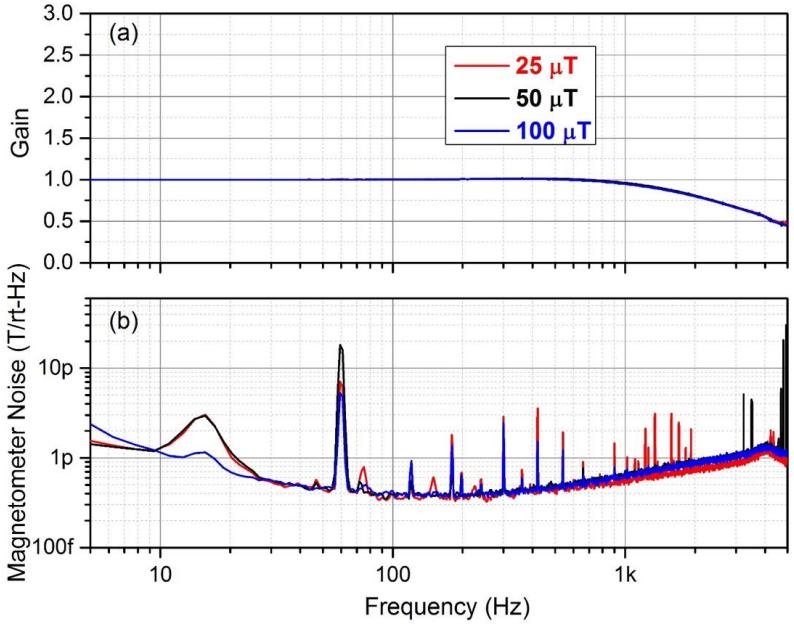

Figure 10 Bandwidth (a) and noise (b) of the magnetometer at different background magnetic fields.

d. Detection of the EM Pulses

In practical applications, we need a signal detecting the onset and the end of EM pulses so that only valid magnetometer readings are reported. In principle, the TDEM system can output a synchronized electronic pulse to be used by the magnetometer as the signal. However, this increases the complexity of the system design integrating both the TDEM instrument and the magnetometer. Therefore, it is preferred that the magnetometer can detect the EM pulse by itself.

The Larmor signal amplitude has a strong response to the onset of EM pulses. When the EM pulse is switched on, the Larmor amplitude is quickly reduced to zero since the PLL cannot follow the EM pulse. After the EM pulse is switched off, the Larmor amplitude will increase when the pump frequency is close to the actual Larmor frequency. This response is used as pulse detector.

We record the root-mean-square (rms) Larmor amplitude as measured by demodulating the probe photodiode signal at the PLL output frequency during the EM pulse. The rms Larmor amplitude (purple curve) together with V_{ref} (blue curve) and the probe Larmor signal (black curve) are plotted in Figure 11 and given by the left axis. The rms amplitude is multiplied by a factor of 10 in order to be on the same scale as the other signals. The magnetometer reading (red curve) is also plotted, given by the right axis. As seen, a threshold in the Larmor amplitude can be used to indicate the onset and the end of the EM pulse.

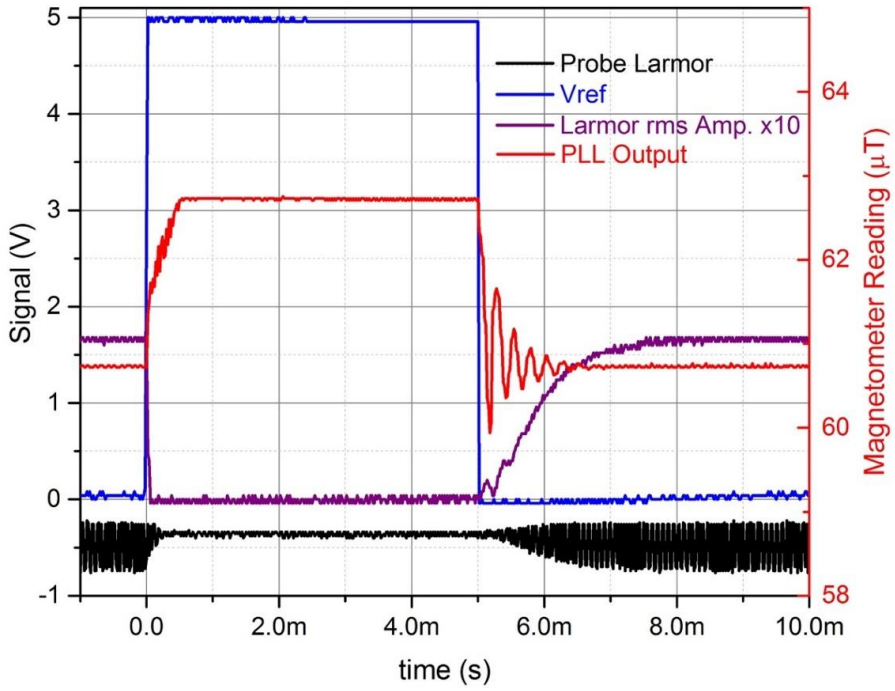

Figure 11 Larmor amplitude in root-mean-square multiplied by 10 (purple curve) during the EM pulse.

e. Discussion

We demonstrate with a bench-top magnetometer that normal operation in presence of a TDEM system is feasible within a millisecond of the magnetic pulse. We also show that the Larmor amplitude can be used as an internal signal to detect the EM pulse, greatly simplifies the design of a practical magnetometer-TDEM system since now they can be operated independently.

Results and Discussion

In the following, we implement the techniques developed in the previous section with a benchtop PLL in the MFAM sensing module. MFAM sensor uses VCSELs instead of DBR lasers as shown in Figure 1. Current modulation is applied to the VCSELs to achieve pump modulation instead of using AOM. These changes enable the miniaturization of the benchtop magnetometer into a sensor package less than 20 cubic centimeters in volume. All signals generated by the sensor are analyzed by a purpose-built digital signal processor (DSP) implemented within a field-programmable gate array (FPGA) that also synthesizes the signals used to drive and control the magnetometer. The basic PLL structure implemented in the DSP is similar as the one shown in Figure 3. As discussed in the previous section, less than one millisecond recovery time is possible. Therefore, the MFAM data sample rate is increased to 3 kHz for this project from the standard 1 kHz. In the following, we present our investigation of fast-recovery with MFAM sensors.

1. Slew Rate of the MFAM

We first test the slew-rate of the MFAM sensor. The sensor is placed inside a magnetic shield can with a constant background magnetic field perpendicular to the optical path of the sensor. Additional 1 μT magnetic field pulses are generated along the same direction. The pulse has a repetition rate of 20 Hz and a duty cycle of 20%. The MFAM readings are recorded with different ramp times of the magnetic field pulse.

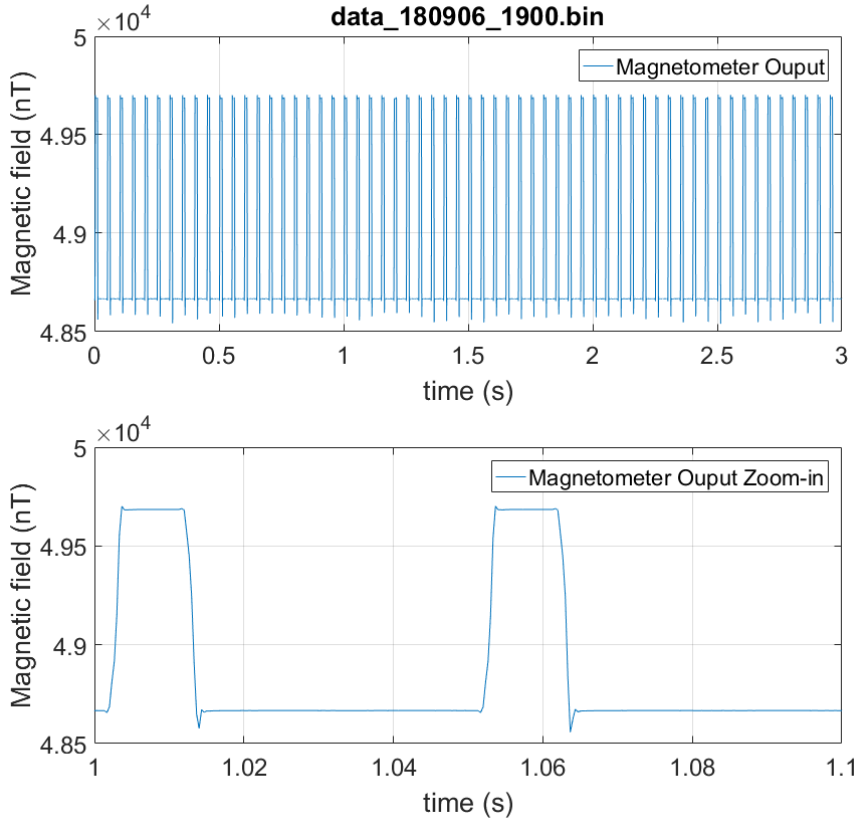

Figure 12 MFAM reading under a magnetic pulse. The pulse has a magnitude of 1 μT, a repetition rate of 20Hz, a duty cycle of 20% and a ramping time constant of 80 μs.

For ramp time greater than 80 μs, MFAM can track the magnetic field pulse robustly, which is shown in Figure 12 for 80 μs ramping time. Overshoot in the response of the output digital filter to a step change in the magnetic field reading can be observed in the zoom-in plot at the pulse edges. PLL dynamics also contributes to the spikes. The MFAM sometimes cannot track the pulse when the pulse ramp time is less than 80 μs, as shown in Figure 13 for a ramping time of 70 μs. In the zoom-in plot, it is clear that magnetometer outputs invalid readings even after the pulse is switched off.

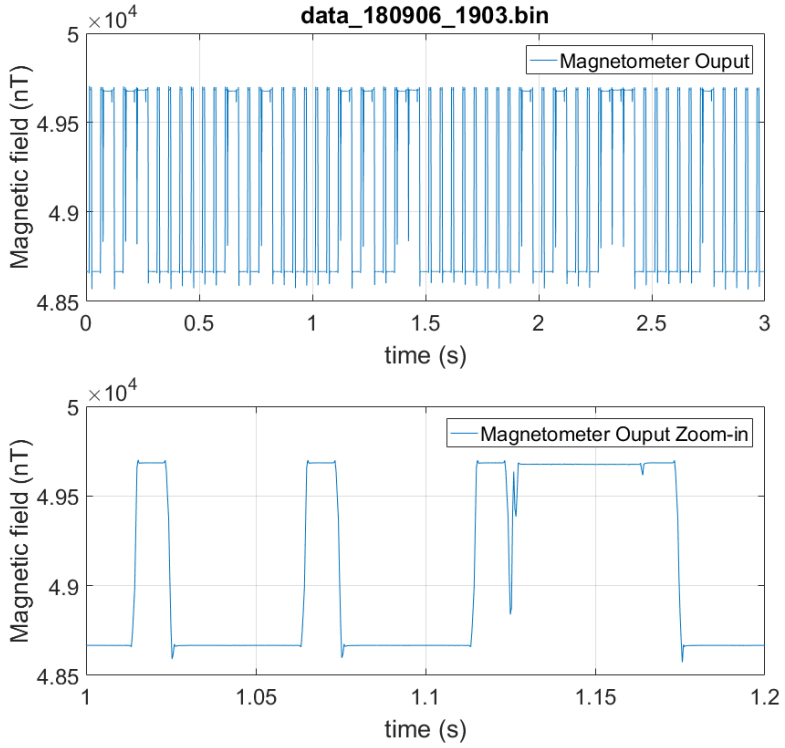

Figure 13 MFAM reading under a magnetic pulse. The pulse has a magnitude of 1 μT, a repetition rate of 20Hz, a duty cycle of 20% and a ramping time constant of 70 μs.

The above experiments indicate a MFAM slew rate of 10 μT/ms, which is much smaller than the slew rate demonstrated in Figure 4 as expected. This is because the bandwidth of the PLL implemented in the MFAM is limited in order to achieve a robust and stable operation in presence of higher measurement noise level from both lasers and driving electronics, The MFAM slew rate, however, is still an order of magnitude higher than that of many commercial magnetometers.

2. Fast-recovery after the EM Pulse in the MFAM

a. Fast-recovery Scheme

The algorithm for fast-recovery after the EM pulse is schematically shown in Figure 14. When the MFAM starts, it scans the full operation range for the Larmor frequency. After the Larmor frequency is found as indicated by the amplitude of the Larmor signal, the PLL is enabled and the magnetometer is in the *Normal Operation* mode. In this mode, the magnetometer

outputs one-millisecond-delayed and appropriately scaled local-oscillator frequency as the field reading and continues measuring the Larmor signal amplitude.

The last valid Larmor frequency is also stored in memory and continuously updated until the probe Larmor amplitude reaches *threshold1*, indicating the onset of the EM pulse at which point the PLL is disengaged. The 1 ms delay is necessary to ensure that the stored Larmor frequency is not affected by the EM pulse. Now the magnetometer enters *Fast Recovery* mode.

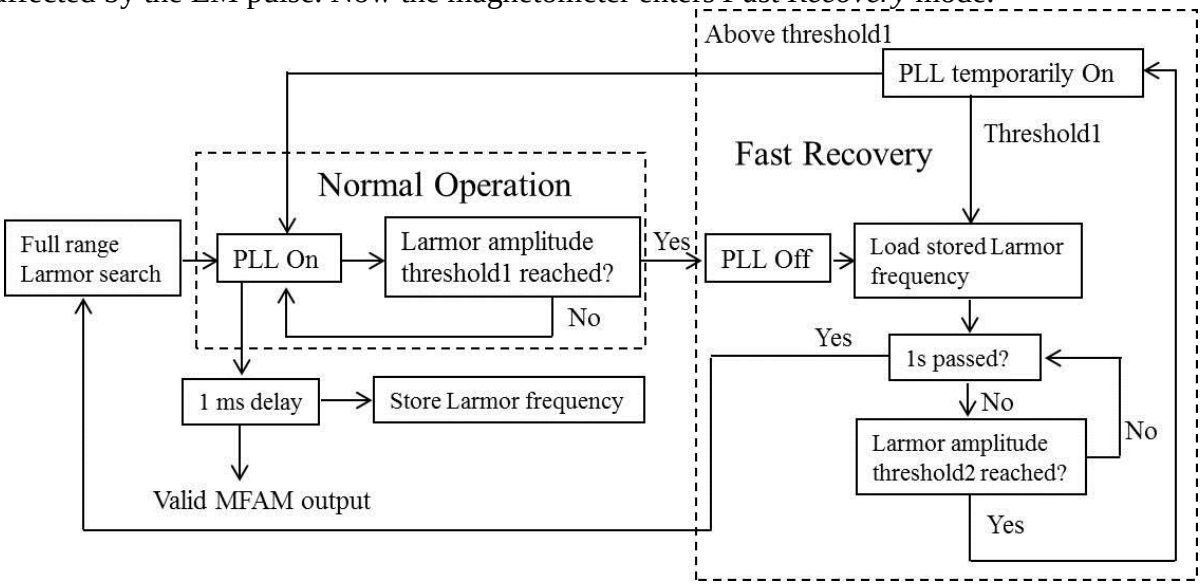

Figure 14 Schematic of the fast-recovery algorithm.

First, the stored Larmor frequency is loaded as the local oscillator frequency (pump modulation frequency). The probe Larmor amplitude is then continuously measured. If it reaches *threshold2*, indicating the end of the EM pulse, the PLL is temporarily engaged for about 50 μs. In this phase, if the probe Larmor amplitude stays above *threshold1*, *Normal Operation* is resumed. Otherwise, the detected signal assumed to be invalid and the magnetometer reenters the *Fast Recovery* mode. *Threshold2* is set to be slightly higher than *threshold1* for robust fast-recovery operation.

A timeout of one second (starting from PLL off) is also set in case of unpredicted failures. We refer the magnetometer reading in *Normal Operation* as valid. In other stages, the magnetometer can also output the local oscillator frequency, which is flagged as invalid and replaced with 0.

b. Fast-recovery with Background Field in Optimal Direction

After implementing the fast-recovery scheme, we first test the sensor in the magnetic shield can with a constant background field (~48.337 μT) perpendicular to the optical path of the sensor. Additional 5 μT magnetic pulse train is generated by an arbitrary function generator through a 5-turn 1-cm-in-diameter coil. The pulses are in the same direction as the background field, with a ramp time of less than 10 μs, a repetition rate of 10 Hz, and a duty cycle of 30%. The slew rate of the pulse is well above the slew rate of the magnetometer.

Valid MFAM readings recorded with the fast-recovery method are shown in Figure 15, where invalid readings replaced by 0. As seen, after the pulse train is turned on around t = 3.1 s, magnetometer recovery during pulse-off is very consistent. In the zoom-in plot, it is also shown

that the noise performance of the magnetometer is not affected by the fast-recovery method. The peak-peak noise in the magnetometer readings is the same before and after the pulse.

To characterize the fast-recovery time, we program the arbitrary function generator to produce a tiny signal during off-time of the pulse train. The signal has FWHM of 0.5 ms and peak amplitude of about 10 nT. The time separation between the signal peak and the falling edge of the pulse is one millisecond. We use an oscilloscope to measure the voltage across a pick-up resistor to record the signal, shown in Figure 16. The oscilloscope is triggered by the falling-edge of the pulse at t = 0. The peak of the signal is at t = 1 ms. Since this signal can be detected by the magnetometer, fast-recovery time of 1ms or less is demonstrated.

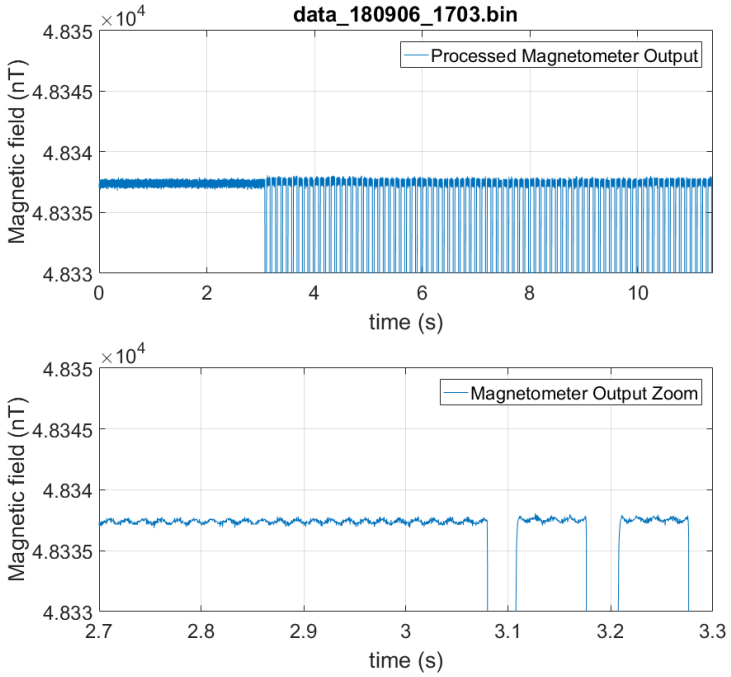

Figure 15 Fast-recovery after magnetic pulses.

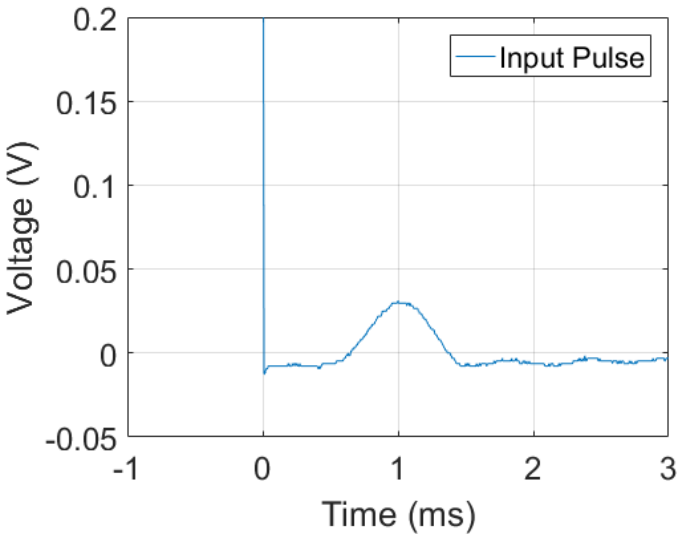

Figure 16 Oscilloscope recording of a tiny signal during pulse-off, starting at t = 0.

Valid magnetometer readings from a pulse train are shown in Figure 17. Compared with the result shown in Figure 15, the applied signal is consistently detected by the magnetometer. Since the magnetometer output and the pulse generation are not synchronized, long-term variation in the envelope of the measured signal amplitude is observed. The measured amplitude variation between adjacent signals is due to small inconsistencies in the fast-recovery time.

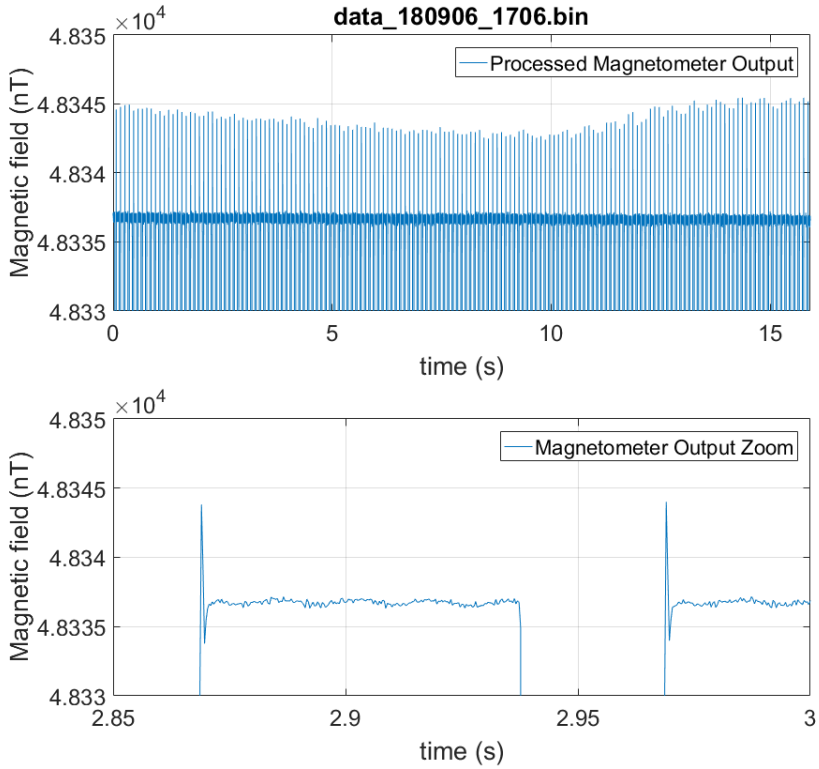

Figure 17 Fast-recovery after magnetic pulses with a tiny signal, as shown in Figure 16, during pulse-off.

Shown in the zoom-in plot in Figure 17, the background field during the signal appears to be several nT lower than the overall background reading. A more careful study indicates that an extra 2 ms is required for the magnetometer reading to settle, as shown in Figure 18, as a result of the PLL control loop dynamics.

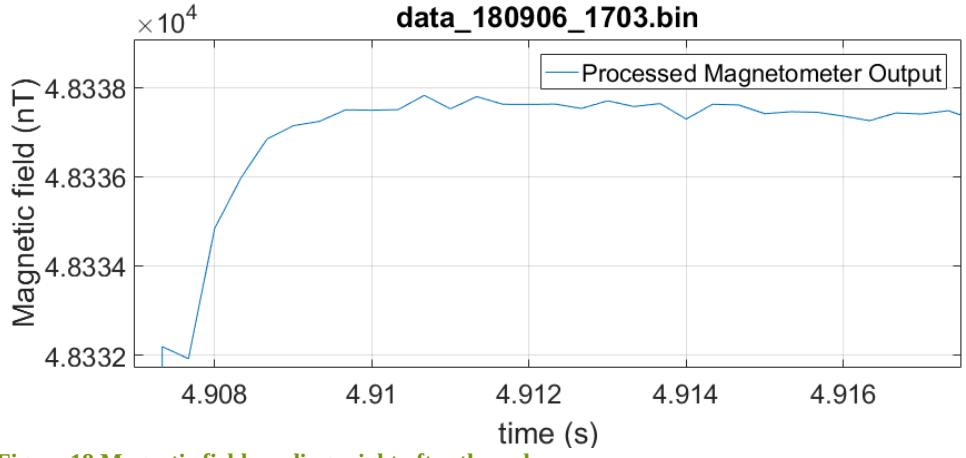

Figure 18 Magnetic field readings right after the pulse.

So far, fast-recovery of the magnetometer in a constant background magnetic field has been verified. In practice, the background field may be slightly different before and after pulses. Since the EM pulses are typically very short (less than 10 ms), that difference can be assumed to be small. In Figure 19 (a), we show the fast-recovery result when the background magnetic field changed by 150nT over the duration of the pulse. As seen, the fast-recovery still works robustly. The fast recovery is verified as before by introducing a small signal during the off-time of the pulse train. The measurement result is presented in Figure 19 (b). As seen, the signal is still detected, indicating a minimal impact of the background magnetic field change on the fast-recovery time. Field changes in the opposite direction are also tested and similar results are observed.

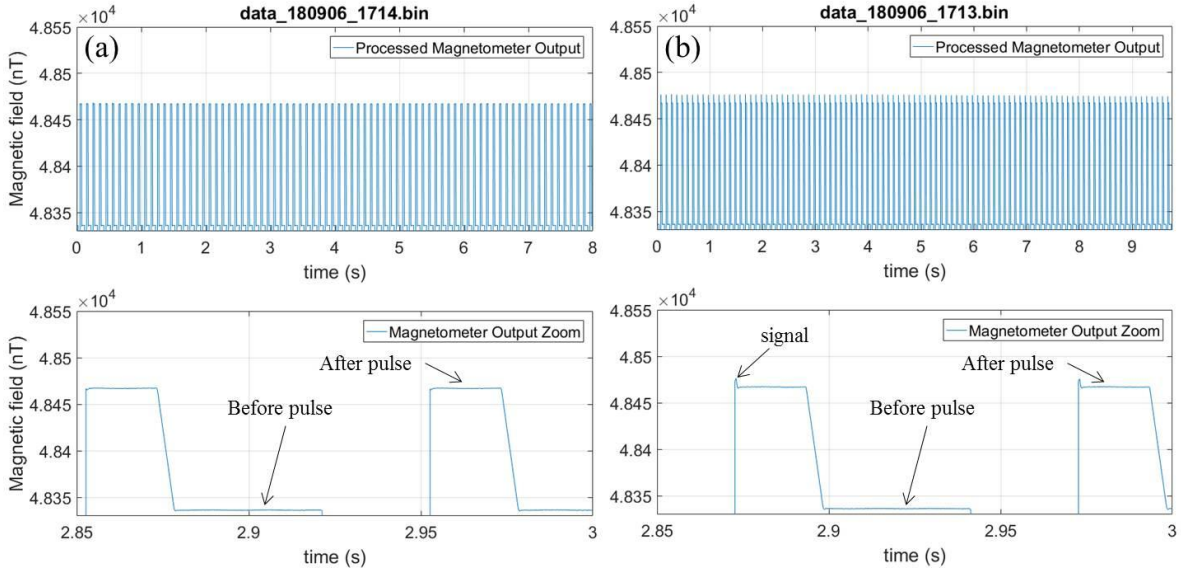

Figure 19 Change of ~150 nT in the background magnetic field before and after the magnetic pulse (a). (b) A tiny signal is added during the pulse-off, with 1 ms between the signal peak and the off-edge of the pulse.

c. Fast-recovery in "Polar 30°" Orientation

The Larmor amplitude depends on the polar angle of the magnetic field, which is defined as the angle between the magnetic field direction and the optical path of the magnetometer. In the previous section, the background magnetic field is set along the optimal direction, 90° polar angle. In practice, this condition is usually not satisfied. As a result, the Larmor amplitude is reduced, which may degrade the performance of the fast-recovery method since it relies on the Larmor amplitude. Hence, the experiments are repeated with the background magnetic field oriented along the "Polar 30°" direction, which on the edge of the dead-zone of the magnetometer with similar results. However, under similar conditions as in Figure 19 (b), the small applied test signal sometimes is not detected, indicating a magnetometer recovery time of more than 1 ms. Increasing the separation between the peak of the signal and the falling edge of the pulse to 2 ms resuts in consistent detection of the signal. The experimental data is shown in Figure 20.

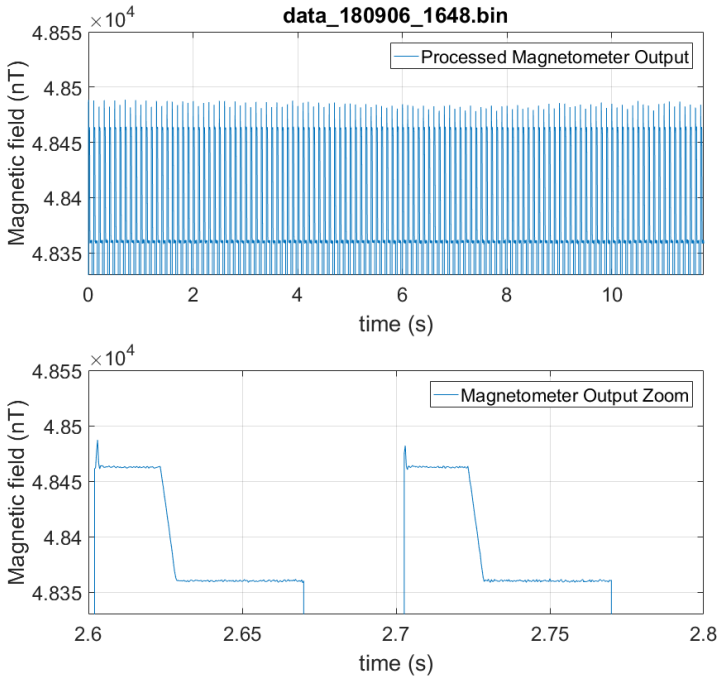

Figure 20 Change of ~100 nT in the background magnetic field (along polar 30° direction) before and after the magnetic pulse (along polar 90° direction). The separation between the off-edge of the pulse and the signal peak is 2 ms.

d. Simultaneous Operation of MFAM with a TDEM System

Field compatibility of the fast-recovery operation is tested by the simultaneously operating the MFAM with a commercially available TDEM system, the MetalMapper from Geometrics. The measurement setup is shown in Figure 21. To simplify the test setup, a magnetic target is displaced relative to the MFAM-MetalMapper system. The MFAM sensor head is placed directly on top of the MetalMapper, maximizing the influence of the EM transmitter pulse train on the magnetometer operation. The sensor orientation is such that the polar angle of the earth's field is about 60°.

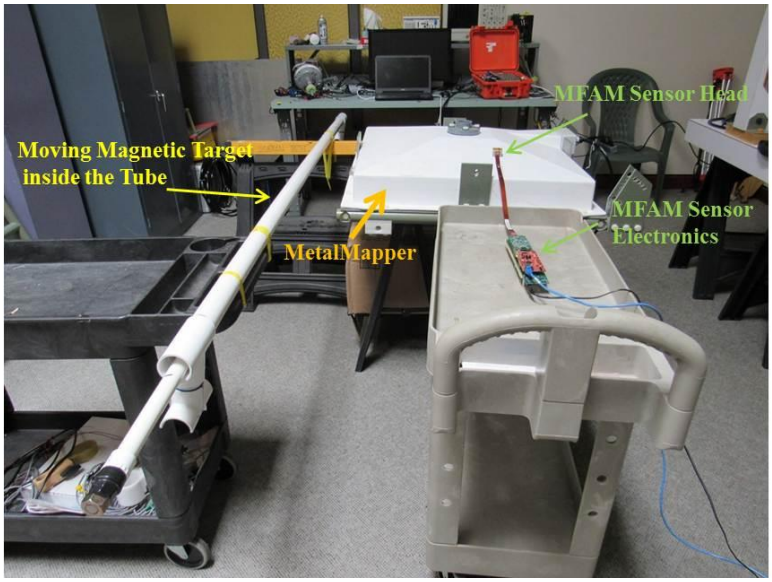

Figure 21 Setup for testing the simultaneous operation of the magnetometer and the MetalMapper.

The MFAM readings are recorded as the pulse train on the transmitter coil of the MetalMapper is switched on and off. At the same time, the magnetic target is moved back and forth in a tube adjacent to the setup, causing a time-varying magnetic anomaly of about 25 nT at the location of the MFAM sensor. When the MetalMapper is transmitting the pulse train, it generates 8 ms pulses of alternating polarity separated by 8 ms off time. Thus, the symmetric bipolar pulse train has a periodicity of 24 ms and duty cycle of 50%. Each pulse has magnetic field amplitude much larger than the Earth's field at the location of the sensor.

The raw MFAM output, including the valid and invalid readings discussed in Figure 14, is plotted in Figure 22 (a). As seen, when the MetalMapper is transmitting, MFAM reading appears to be very noisy, overwhelming any magnetic field signal. After the MetalMapper is switched off, the effect of the moving magnetic target is clearly visible. The noise in the MFAM readout during MetalMapper pulse off time is dominated by 60 Hz powerline field.

If the MFAM recovery time is much less than 8 ms, an internal signal can be used to distinguish between valid and invalid readings. Thus, the disturbance caused by the MetalMapper pulses can be masked out and the magnetic field from the moving target can be recovered from the raw data. In Figure 22 (b), we plot only the valid readings of the same data as in Figure 22 (a). Masked data indicates that turning on the MetalMapper almost has no effect on the MFAM operation. Note that here we mask additional 2 ms data, as discussed in Figure 18. Otherwise, the signal appears a little bit noisier when the MetalMapper is transmitting the pulse train.

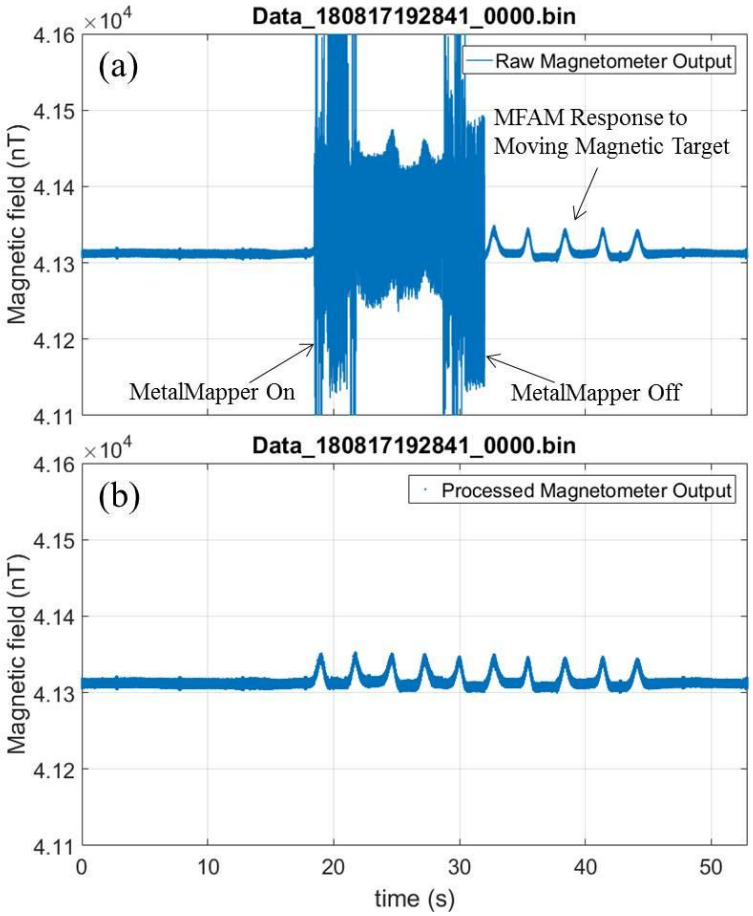

Figure 22 MFAM readings during on and off of the MetalMapper. (a) Raw MFAM output including valid and invalid readings. (b) The same data as in (a), but only valid readings are plotted.

e. Discussion

Here, we have experimentally validated that the MFAM can respond to magnetic field changes less than 1 ms after the EM pulse is switched off. When measuring a magnetic signal smaller than 10 nT, an additional 2 ms of recovery time might be necessary. We also set up a composite MFAM-MetalMapper system and successfully verified the simultaneous operation of the MFAM with the commercial TDEM system. With the fast-recovery method, the negative effect of the EM pulse on the MFAM operation is shown to be mitigated. We expect the fast-recovery to function well as long as the frequency of the TDEM system is less than 100 Hz, i.e. the off-time of the EM pulse is more than 2.5 ms assuming bi-polar EM pulses.

3. Measurement during the EM Pulse

a. Fast-recovery Scheme

The procedure for measurement during the pulse is schematically shown in Figure 23. Here *Normal Operation* and *Fast Recovery* procedures are essentially the same as shown in Figure 14. When the MFAM starts, it scans the full operation range for the Larmor frequency. After the Larmor frequency is found, it is stored, and *Normal Operation 1* commences.

If the Larmor signal is lost during *Normal Operation 1*, magnetometer operation enters *Fast Recovery 1*, where the starting frequency for the local oscillator is the calculated Larmor frequency based on the angle measurement that is updated every 10 ms. If *Fast Recovery 1* succeeds within about 1 ms, *Normal Operation 2* follows. *Normal Operation 2* is in principle the same as *Normal Operation 1*, except that when it fails, magnetometer enters *Fast Recovery 2*.

In *Fast Recovery 2*, the starting frequency for the local oscillator is the stored Larmor frequency. If *Fast Recovery 1* fails after about 1 ms, *Fast Recovery 2* is tried, and vice versa. If the magnetometer does not resume normal operation (either 1 or 2) after one second, the MFAM starts scanning for the Larmor frequency again over its full dynamic range of 20μT to 100μT.

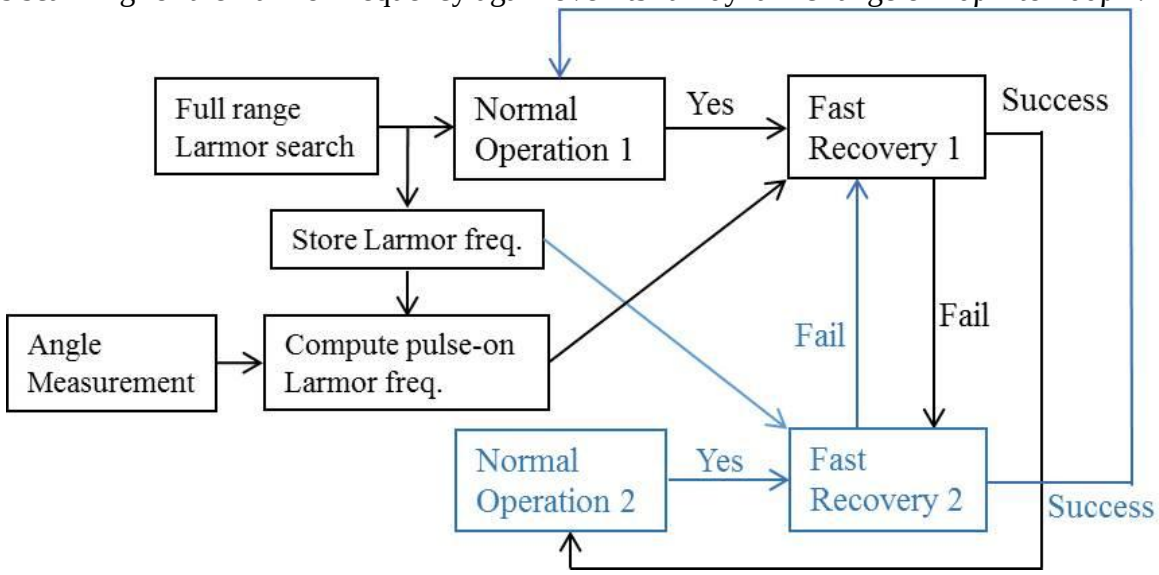

Figure 23 Schematics showing the measurement method during EM pulses.

The MFAM cannot detect the polarity of the EM pulse. Therefore, the calculated Larmor frequency may be incorrect. To solve this problem, if two consecutive normal operations are in

Normal Operation 1(meaning that the fast-recovery-during-pulse does not work), the opposite pulse polarity is assumed for the Larmor frequency calculation.

In many practical applications, the EM pulse keeps switching its polarity. In such cases, the MFAM hardware can be modified to accept a trigger from the TDEM system. The above algorithm can then be extended to beyond two states. Multiple states corresponding to multiple field values can be sequenced using the trigger input. Algorithms can be implemented to accept a sequence of field values after the trigger pulse, and the angle measurement method can be used to scale the field values for a known geometry to expand to multiple states.

b. Verification in the Magnetically Shielded Environment

We first verify the previously described algorithm for measurement of magnetic field during an EM pulse inside the magnetic shield can. The EM pulse is oriented along the optical path of the magnetometer and calibrated to be about 5 μT with less than 10 μs ramp time. The unipolar pulse is on for 5 ms and with a repetition rate of 50 Hz. Its polarity can also be switched. In this pulse configuration, only the polar angle of the background magnetic field is needed for calculating the Larmor frequency during the pulse.

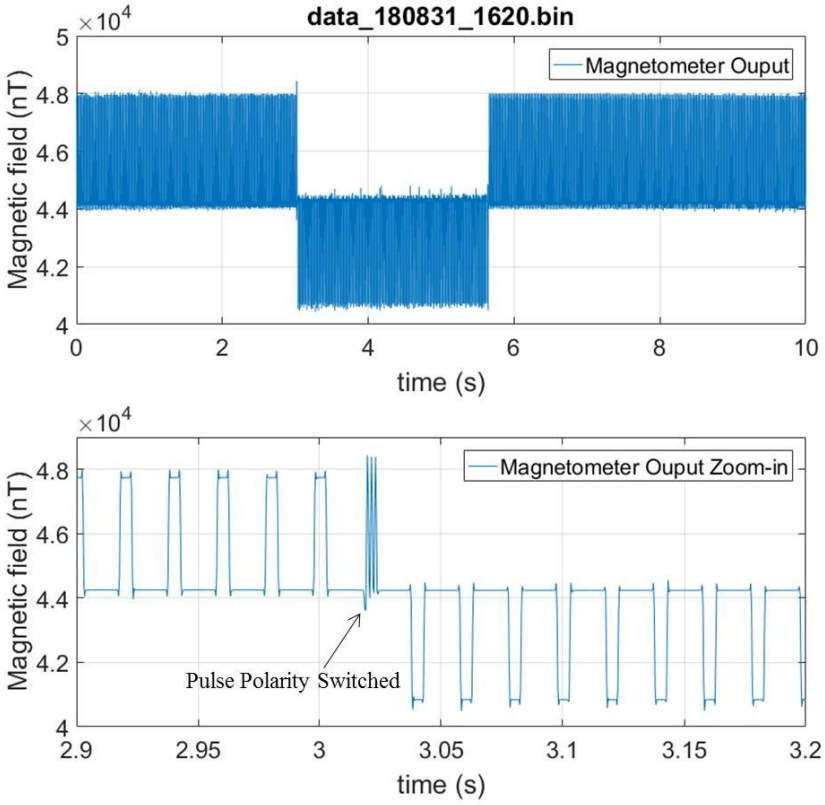

Figure 24 Measurement during EM pulses. The pulse is along the optical path (polar 0°) of the MFAM sensor and the background magnetic field is along polar 30°. Both valid and invalid readings are plotted.

The fast-recovery method is tested for many background magnetic field directions. Measurement during and after the pulse is observed in reliably repeatable manner. The experimental data with the background magnetic field oriented along polar 30° angle is shown in Figure 24. Over many cycles, the fast-recovery method does not fail except right after the pulse polarity is switched, as shown in the zoom-in plot. When the pulse polarity is switched, the

calculated Larmor frequency during the pulse is no longer correct in which case the measurement during the pulse does not work.

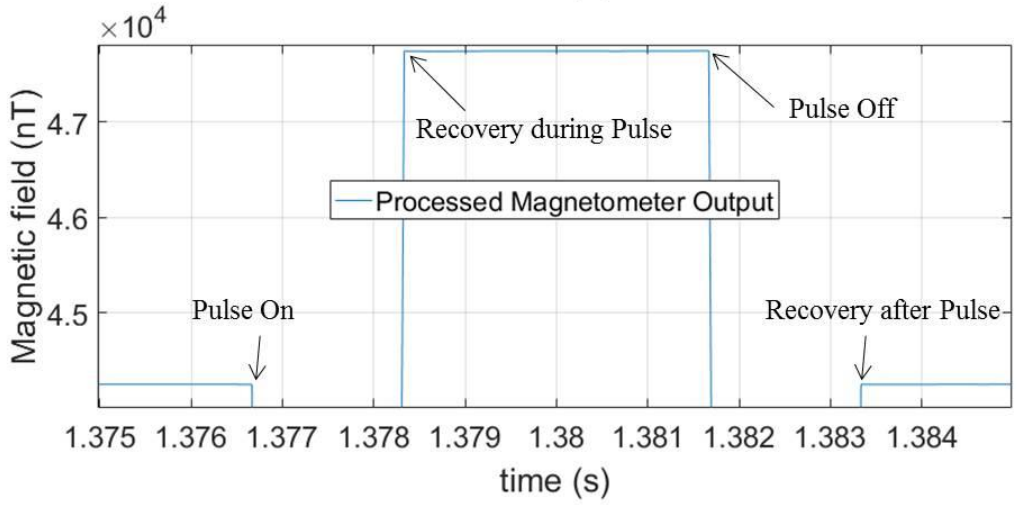

Figure 25 Zoom-in plot of the data shown in Figure 24. Only valid readings are shown here.

As discussed in the above section, after two consecutive fast recoveries in *Normal Operation 1*, the opposite polarity is assumed, and the measurement can be subsequently made. Since both pulse polarities are taken into account in the fast-recovery algorithm, only polar 0° to 90° is needed in the angle measurement. Polar 90° to 180° with one pulse polarity gives the same answer as polar 0^o to 90^o with the opposite pulse polarity. In Figure 24, both valid and invalid readings are plotted.

To measure the fast-recovery time, we zoom into a single-pulse duration within the data shown in Figure 24 and plot only the valid readings in Figure 25. As shown, both recovery times during and after the pulse are a little less than 2 ms. This recovery time is longer than that for the fast-recovery-after-pulse method, mainly due to the increased complexity of the recovery scheme. We expect the recovery time to be reduced if a trigger input heralding the EM pulse can be used to simplify the fast-recovery scheme.

c. Measurement during the EM Pulse in the Open Environment

We also test the measurement-during-pulse method outside the magnetic shield can. The setup is shown in Figure 26. The EM pulse is generated by an arbitrary waveform generator through two 5-turn coils wrapped around the MFAM sensor head. The magnetic pulse is along the optical path (polar 0°) of the MFAM sensor and has amplitude of 5 μT, repetition rate of 10 Hz and a duty cycle of 50%. When the pulse is on, the sensor head is also rotated randomly in order to simulate the instrument orientation change during surveys.

Magnetometer readings are recorded, and the results are shown in Figure 27. When the sensor is rotated, the total magnetic field at the location of the sensor changes since the pulsed magnetic field vectorially adds with the earth's field. This effect can be seen from the pulse envelope in Figure 27. When the earth's field is close to polar 90°, the projection of the pulsed field along the earth's field is almost negligible. When the sensor is oriented such that the earth's field is on the edge of the sensor dead-zone, the projected pulsed field has the highest amplitude.

Angle measurement ensures that the calculated Larmor frequency for the pulse-on duration is accurate enough throughout the rotation of the sensor. We also rotate the sensor through the

dead-zone. In one case, the sensor stays in the dead-zone for more than two seconds, forcing MFAM to restart the scan for Larmor frequency over the full dynamic range. In the second case, the sensor goes through the dead-zone within one second. In both cases, MFAM recovers its operation once outside the dead-zone.

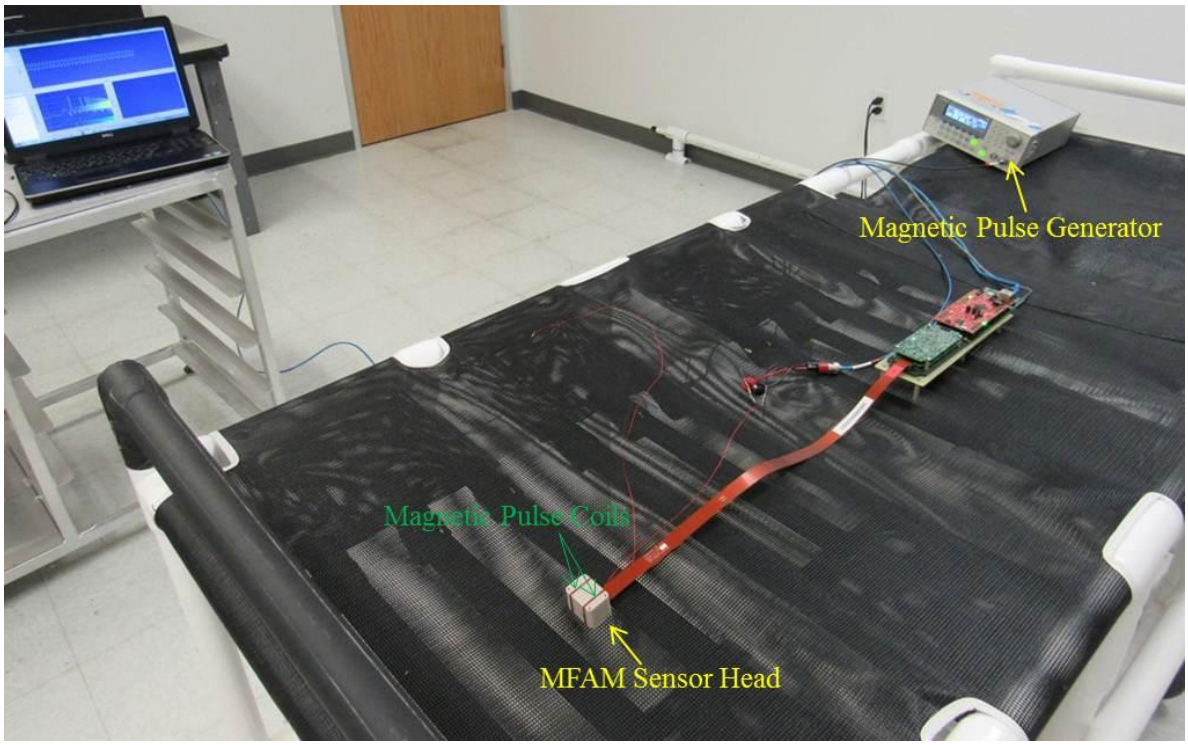

Figure 26 Experimental setup for testing the fast-recovery-during-pulse method in the open environment.

Opposite pulse direction is also tested by quickly switching the sensor to the opposite orientation. As seen in the zoom-in plot, after one pulse cycle, the magnetometer recovers its operation during pulses. Small oscillating signal due to powerline is present during both pulse-on and pulse-off. Detection of powerline magnetic field confirms that the magnetometer is functioning both during and after pulses.

d. Discussion

In this section, we demonstrate magnetic field measurement during EM pulses. Angle measurement result is used to calculate the starting Larmor frequency for fast-recovery during the pulse with less than 2 ms recovery time observed. We also emulate field operation by rotating the sensor and the EM coil in the earth's magnetic field. Reasonably robust operation of fast-recovery during EM pulses is demonstrated. In practical applications, the EM pulses generate much bigger magnetic fields than 5 μT tested here. However, as discussed before, for any useful interpretation of the field reading during the pulse, the EM pulse has to be locally compensated at the location of the sensor. The pulse field after compensation should ideally be much less than 5 μT. Otherwise the heading error during the pulse is too much, as demonstrated in Figure 27.

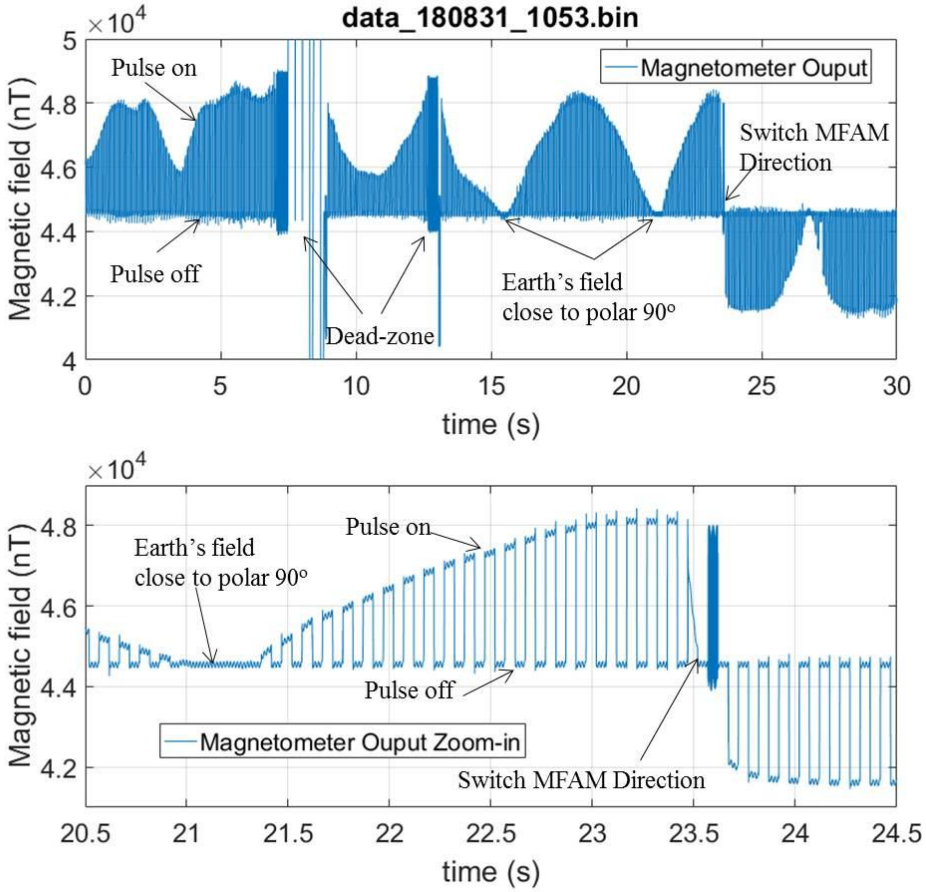

Figure 27 Fast-recovery during EM pulses in an open environment. The data is taken when the MFAM is rotated.

4. Towards Field Applications

a. Challenges in Field Applications

There are two main challenges in using MFAM sensors in real-world field applications: dead-zone and heading-error. The strength of the magnetic sensing signal (Larmor signal), depends on the relative angle between the optical path of the sensor and the background magnetic field. The signal strength decreases and eventually vanishes as the optical path of the sensor approaches the background magnetic field direction. This is called polar dead-zone. The MFAM sensors have a polar dead-zone of about ± 25° with respect to the optical path.

Even when the sensor is outside the dead-zone, the magnetic field reading of the sensor slightly depends on the orientation of the sensor relative to the background magnetic field. This is called heading error of the sensor. Many factors contribute to the heading-error, such as nonlinear Zeeman-shift of alkali atoms, light-shift effect [4], and orientation-dependent phase change in Larmor signal.

In Figure 28, we show a typical measurement of the dead-zone and the heading-error of MFAM sensors. The optical axes of two sensors are initially aligned along the background magnetic field direction, as shown in Figure 28 left. The sensors are then rotated with the rotation axis perpendicular to the field. The change in magnetic field readings of the sensors is measured as a function of rotation angle and shown in Figure 28 right.

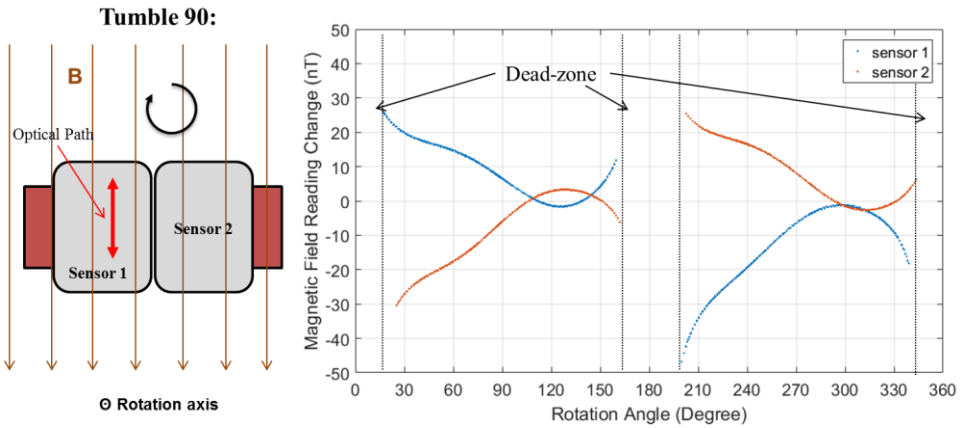

Figure 28 Measurement of the dead-zone and the heading-error. Left: schematic showing the rotation of the sensor in the background magnetic field. Right: sensor output (with a constant offset) as a function of sensor rotation.

As seen, when sensor optical axes are aligned close to the magnetic field direction, the sensors are in the dead-zone and do not produce valid field readings. Outside the dead-zone, although the background magnetic field does not change, the sensor field readings still vary due to the heading-error. Typical heading-error is about 60 nT.

b. Solution and Results

MFAM control electronics can operate two MFAM sensors at the same time. Therefore, we can orient two sensors orthogonally, as shown in Figure 29, and combine the Larmor signals of two sensors as a single signal input. In this configuration, the combined Larmor signal will never approach zero under any sensor orientation since one of the two sensors will always be outside its dead-zone. It turns out that the heading-error of the combined sensor is also much smaller than that of individual sensors shown in Figure 28. The magnetic field gradient tolerance of the combined sensor, however, is greatly reduced to about 10 nT/cm. Nevertheless, in most field applications, the background magnetic field gradient should still be within this limit.

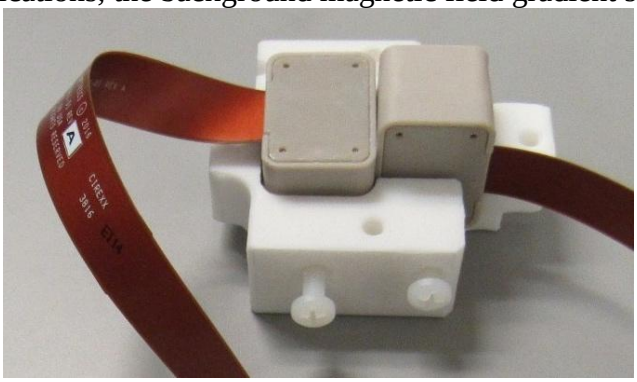

Figure 29 Orthogonal orientations of two sensors for dead-zone-free operation by combining the signal inputs of two sensors. The heading-error in the combined operating mode in this configuration is also greatly reduced.

We perform similar measurements to the one shown in Figure 28 with the combined sensor. Three orthogonal rotation axes are chosen such that during each rotation the optical axis of at least one sensor will be oriented along the background field. In the single sensor mode, this causes the sensor to enter the dead-zone. However, due to the orthogonal configuration of two sensors, the other sensor should be at the optimal orientation with its optical axis perpendicular to the magnetic field.

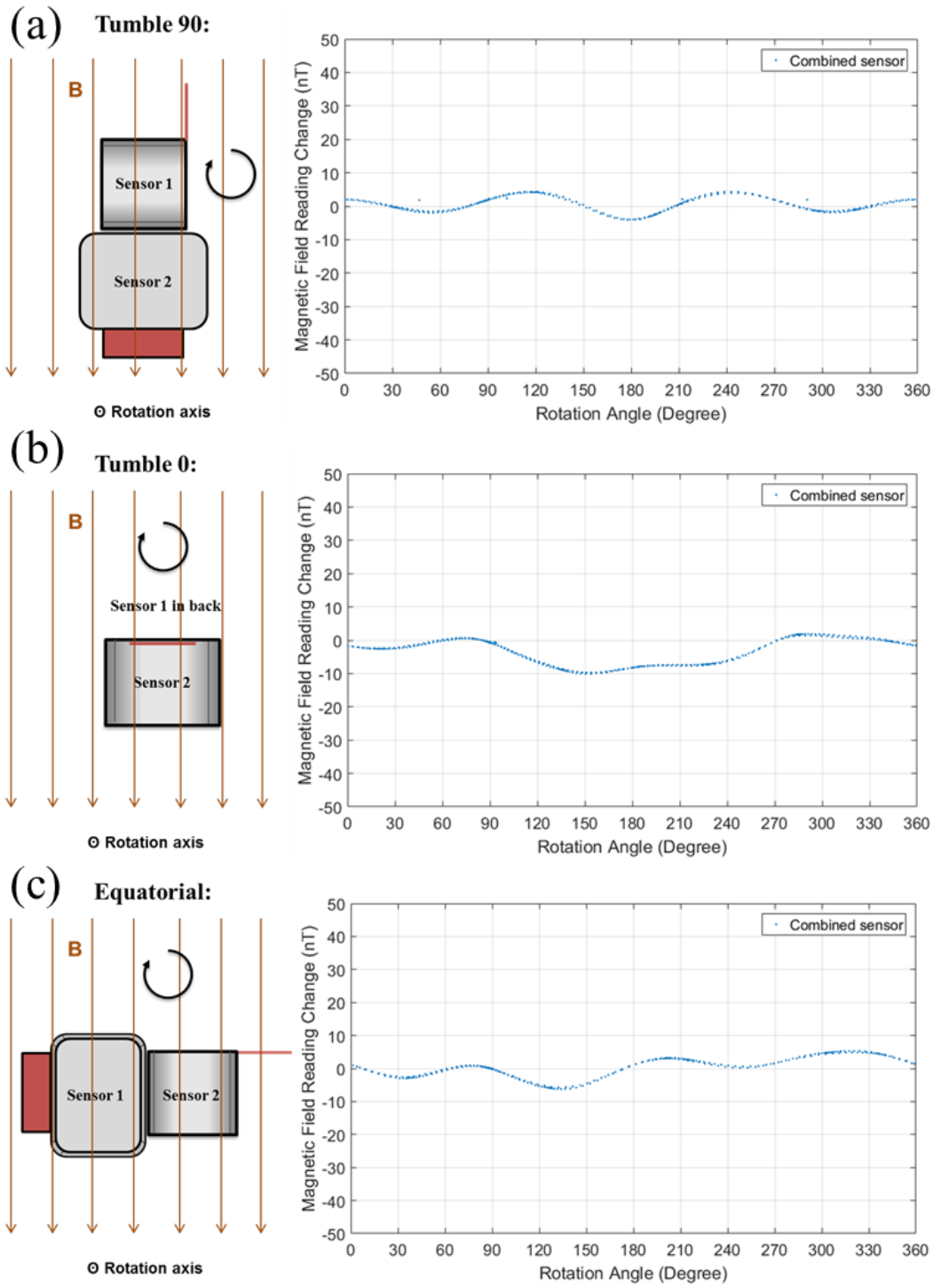

Figure 30 Heading-error measurements of the combined sensor. Three different rotation axes are chosen such that during the rotation at least one sensor optical axis can overlap with the magnetic field.

The dead-zone and heading-error measurement results around the three orthogonal rotation axes are plotted in Figure 30. The two sensors used here are the same as the ones in Figure 28. As shown, the combined sensor has no dead-zone. The heading-error is also greatly reduced from 60 nT to about 12 nT, a factor of 5 improvement. The heading-error reduction is achieved mainly by cancelling out the orientation-dependent phases when the two Larmor signals are

combined, and by avoiding the sensor operation close to dead-zone where the magnetic reading is affected most by signal perturbations since the Larmor signal is small.

c. Fast-recovery Time of the Combined Sensor

We perform the same measurement as shown in Figure 17 to verify that the fast-recovery time is not affected by the combined operation of two sensors. The result is shown in Figure 31. As seen, small signals applied after large magnetic pulses can be detected. This demonstrates that the fast-recovery time of the combined sensor is still less than 1 ms, same as the single sensor.

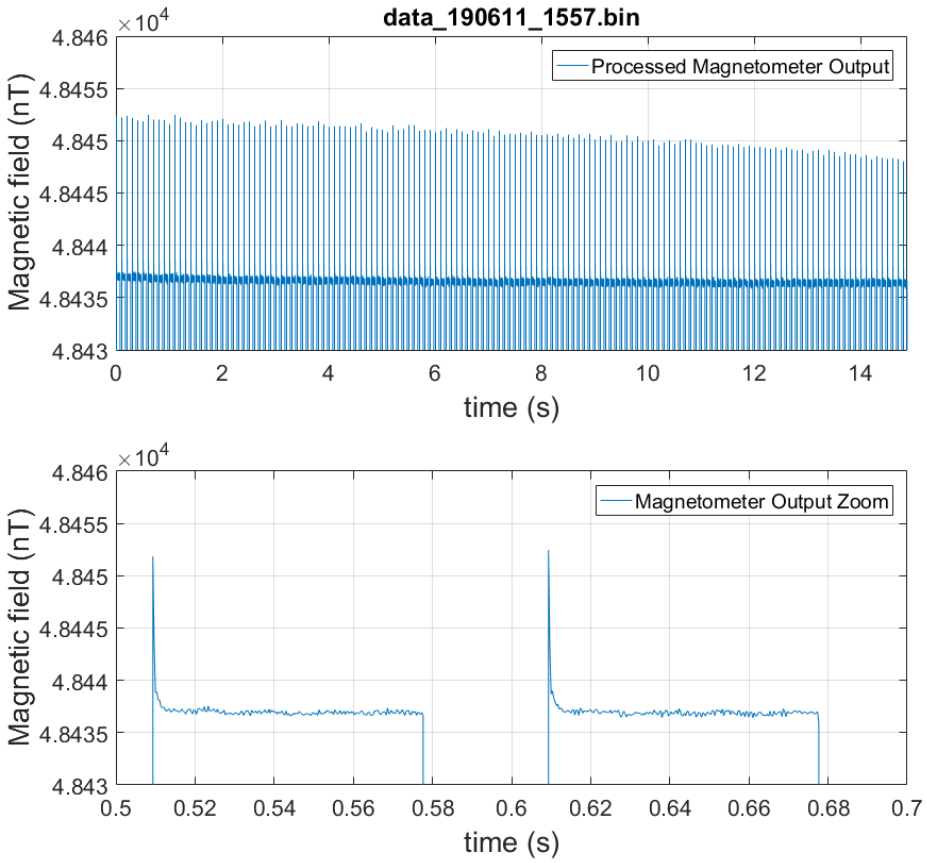

Figure 31 Fast-recovery of the combined sensor after magnetic pulses. The experimental conditions are the same as those in Figure 17.

d. Discussion

In this section, we identify dead-zone and heading-error as two possible issues when applying the fast-recovery technique using a single MFAM sensor to real-world field applications. By operating two orthogonal sensors in a combined mode, we demonstrate that these two issues can be considerably mitigated. The fast-recovery time is also shown to be not affected by the combined operation of two sensors.

Conclusions to Date

In conclusion, we have demonstrated the fast-recovery of MFAM operation in presence of EM pulses. The Fast Recovery algorithm is first implemented in MFAM DSP. The magnetometer is shown to respond to a small signal less than one millisecond after the EM pulse is switched off, when operating in the optimal background magnetic field direction. Less than two milliseconds recovery time can be expected over the entire operating orientations of the magnetometer in the earth's magnetic field.

We also successfully demonstrate the simultaneous operation of MFAM with a commercial TDEM system while minimizing the negative effect of the EM pulse on MFAM operation. We expect MFAM to function normally as long as the pulse frequency of the TDEM system is less than 100 Hz, i.e. the off-time of the EM pulse is more than 2.5ms assuming bipolar pulses. Prior projects investigating simultaneous magnetometer and EM system operation [1, 5, 6] required interleaving magnetometer and EM system data acquisition. In our method, the magnetometer and the EM system can be operated independently, which greatly simplifies the system integration of the two devices into a fieldable instrument. In addition, the combined system can have much higher sample rate than that the prior projects have been able to demonstrate.

By combining the angle measurement method, developed in the Task 1 of the MR-2646 project along with the fast-recovery method, MFAM can now be operational during EM pulses. Reasonably robust operation is demonstrated even when the integrated system of MFAM and the EM coil is rotated in the earth's magnetic field. The newly-developed capability of MFAM can greatly facilitate practical applications in UXO detection and discrimination. This topic will be explored in the Task 3 of the project.

Finally, we address two issues of MFAM sensors, dead-zone and heading-error, in field applications. We successfully demonstrate the solution to these two issues by combining the signals from two orthogonal sensors in preparation of field tests.

References

[1] R. Siegel, "Combined Electromagnetic and Magnetometer Data Acquisition and Processing," ESTCP Project MM-0208, 2004.

[2] D. Budker and D. F. J. Kimball, Optical Magnetometry, Cambridge: Cambridge University Press, 2013.

[3] W. E. Bell and H. L.Bloom, "Optically driven spin precession," *Phys. Rev. Lett.*, vol. 6, p. 280, 1961.

[4] H. T. a. W. H. B. S. Mathur, "Light shifts in the alkali atoms," *Phys. Rev.*, vol. 171, p. 11, 1968.

[5] R. Siegel and R. Selfridge, "Man-Portable Simultaneous Magnetometer and EM System (MSEMS)," ESTCP Project MM-0414, 2008.

[6] R. M. Siegel and K. D. Enriquez, "Underwater Simultaneous EMI and Magnetometer System (USEMS)," ESTCP Project MR-200733, 2011.